

2012

The effect of stochastic nano-scale surface roughness on microfluidic flow in computational microchannels

Robert Jaeger
Iowa State University

Follow this and additional works at: <https://lib.dr.iastate.edu/etd>

 Part of the [Mechanical Engineering Commons](#)

Recommended Citation

Jaeger, Robert, "The effect of stochastic nano-scale surface roughness on microfluidic flow in computational microchannels" (2012).
Graduate Theses and Dissertations. 12678.
<https://lib.dr.iastate.edu/etd/12678>

This Thesis is brought to you for free and open access by the Iowa State University Capstones, Theses and Dissertations at Iowa State University Digital Repository. It has been accepted for inclusion in Graduate Theses and Dissertations by an authorized administrator of Iowa State University Digital Repository. For more information, please contact digirep@iastate.edu.

The effect of stochastic nano-scale surface roughness on microfluidic flow in computational microchannels

by

Robert Joseph Jaeger

A thesis submitted to the graduate faculty
in partial fulfillment of the requirements for the degree of
MASTER OF SCIENCE

Major: Mechanical Engineering (Thermo-Fluid Sciences)

Program of Study Committee:
Baskar Ganapathysubramanian, Major Professor
Michael G. Olsen
Sriram Sundararajan

Iowa State University

Ames, IA

2012

DEDICATION

I would like to dedicate this thesis to my mother Gwen and my father Jim without whose unconditional moral and financial support I would not have been able to complete this work. I would also like to dedicate this thesis to my siblings Alicia, Chris, and Jon who have always been formative role models throughout my life.

TABLE OF CONTENTS

LIST OF FIGURES	v
LIST OF TABLES	vii
ABSTRACT.....	viii
CHAPTER 1. GENERAL INTRODUCTION	1
Microchannels in Biomedical Devices.....	1
Research Motivation	2
Thesis Organization.....	3
References	4
CHAPTER 2. NANO-SCALE SURFACE ROUGHNESS AFFECTS LOW RE FLOW: EXPERIMENTS AND MODELING	5
Abstract	5
Introduction	5
Experimental Setup: Fabrication, characterization, and visualization	7
Modeling Framework: Mesh generation and solution technique.....	9
Results and Discussion.....	10
Conclusions and Outlook	15
References	15
CHAPTER 3. INVESTIGATING THE EFFECT OF NANO-SCALE SURFACE ROUGHNESS ON MICROFLUIDIC NEWTONIAN FLUID FLOW	20
Abstract	20
Introduction	21
Computational Domain Construction.....	26
Microchannel Roughness: Experimental Manufacturing	27
Microchannel Roughness: Characterization	29
Governing Equations: Newtonian Fluid	30
Validity of Continuum Hypothesis.....	31
Validity of No-Slip Boundary Condition	31
Computational Methods	33
CFD Microchannel Grid.....	33

Flow Rate Determination.....	33
Solution Framework	34
Periodic Boundary Conditions.....	36
Results and Discussion.....	36
Conclusions	42
References	43
CHAPTER 4. GENERAL CONCLUSIONS.....	47
General Discussion.....	47
Recommendations for Future Research	48
General Recommendations.....	48
Non-Newtonian Fluid Recommendation.....	48
References	50
APPENDIX A. MICROCHANNEL AND SURFACE CREATION.....	52
APPENDIX B. AUTOCORRELATION FUNCTIONS	58
ACKNOWLEDGEMENTS	60

LIST OF FIGURES

Figure 1. Example of lab-on-a-chip medical device by (Ahn et al. (2004)).....	1
Figure 2. Examples of (a) deliberate roughness (McUsic et al. (2012)) and (b) stochastic roughness (Young et al. (2011)) on experimental microchannel surfaces.	2
Figure 3. The geometry and mesh detail of the computational microchannel domain. The roughness height on the zoomed-in section is exaggerated for clarity. The width of the channel is $460\mu\text{m}$ at the rough surface.	9
Figure 4. Autocorrelation lengths (ACL) of experimental and CFD v-velocity-component perturbations for both etched and un-etched surfaces at all flow rates, Q [ml/min].	12
Figure 5. Energy spectra analysis of u-v-w velocity perturbation sum of squares: energy spectra of the velocity field as a function of flow rate (a) at $7.82\mu\text{m}$ above the rough surface of etched glass, and the energy spectra (b) of $Re = 6.5$ of etched and un-etched	13
Figure 6. V-velocity component contour plots of (a) $Re = 0.06$ un-etched, (b) $Re = 0.06$ etched, (c) $Re = 6.5$ un-etched, and (d) $Re = 6.5$ etched (fluid flow goes from left to right). The xz-plane slices were taken $175\mu\text{m}$ away from the microchannel side wall.....	14
Figure 7. Example microchannel in medical device by Chen et al. (2003)	22
Figure 8. Computational microchannel domain geometry with mesh details.	26
Figure 9. Height contours [μm] of the etched surface used in the computational domain.	27
Figure 10. Histogram of the surface heights for (a) un-etched and (b) etched surfaces.	28
Figure 11. Measured contact angles of water on un-etched glass (a) and etched glass (b). The contact angles prove they are both hydrophilic surfaces.	32
Figure 12. V-velocity contours in the xz-plane (depicted in the shaded red region above) of etched and un-etched glass surfaces for the same Reynolds number.	37
Figure 13. W-velocity contours in the xz-plane of etched and un-etched glass surfaces for the same Reynolds number.....	37

Figure 14. V-velocity contours in the xz-plane for an etched glass surface for all tested Reynolds numbers.....	38
Figure 15. Autocorrelation length (ACL) as a function of height above the rough surface of the (a) v-velocity and (b) w-velocity perturbations in the xy-plane.....	40
Figure 16. Energy spectra of (a) uvw-velocity perturbations as a function of Reynolds number $7\mu\text{m}$ above the rough surface and (b) the uvw-velocity perturbations in the xy-plane as a function of height above the rough surface.....	41
Figure 17. Sequential process to manufacture the experimental microchannel with etched glass as the bottom surface.....	52
Figure 18. Sample optical profilometer surface scans of un-etched glass (left) and etched glass (right).....	53
Figure 19. Consecutive surface scans with a sample test region (shaded in red)	55
Figure 20. Consecutive surface scans showing the true overlapping regions (shaded)	55
Figure 21. Three consecutive surface scans seen stitched together with dotted lines showing the original scans	56
Figure 22. Final etched microchannel surface with three consecutive images.	57

LIST OF TABLES

Table 1. Comparison of experimental and DNS metrics at 25 μm from rough surface [μm].	11
Table 2. Fluid properties of water used in CFD simulation.	33
Table 3. Fluid properties of non-Newtonian blood analog fluid KSCN-X solution by Gijssen et al. (1999).	50

ABSTRACT

Microfluidics is a promising technology that is used extensively in biomedical devices, so called lab-on-a-chip devices. These devices harness a network of microchannels to mix, react, and conduct fluid flow. Most microchannel fabrication methods produce a stochastic surface roughness with heights ranging in the micro- to nano- scale. This inherent, stochastic roughness can potentially be harnessed to enhance microfluidic operations. Previous research on rough surfaces in microfluidics has focused on periodic, micro-scale obstructions, not of any stochastic nature. The purpose of this research is to characterize the effect of stochastic nano-scale surface roughness on microfluidic flow using very large-scale direct numerical simulations (DNS) and micro- particle image velocimetry (micro-PIV).

The two studies are focused on a microchannel with one of the walls, the bottom surface, which has a manufactured surface roughness using a hydrofluoric-acid (HF) etching process. The rough surface is scanned by an optical profilometer, and the exact topography is imported as the bottom surface of the computational microchannel. HF-acid etched glass and un-etched glass surfaces are directly compared to each other. In the first study, the DNS simulations are compared to micro-PIV experiments for a Newtonian fluid (water). The flow regime was laminar, diffusion dominated and limited to $Re < 10$.

The second study used a longer microchannel relative to the first study that was made possible by stitching together consecutive profilometer surface scans. This study only used simulations to study the effect of nano-scale roughness on microfluidic flow (with the previous study forming a basis for model validation). In the future, the study will be extended to Newtonian as well as non-Newtonian (shear-thinning) fluids in the same flow regime as the first study.

Overall, we have shown that an experimentally validated and experimentally driven three-dimensional computational study for microfluidic stochastic surface roughness is possible. Additionally, we have shown that the stochastic nature of the surface roughness and its effect on fluid flow can be characterized with numerous tools including velocity-perturbation contours, autocorrelation length (ACL), and energy spectra analysis.

The different analyses illustrated the effect of the rough surface in different ways. Velocity-perturbation contours show that both the etched and un-etched rough surfaces produce very small velocity structures (eddies) very near the rough surface that merge to form larger structures as the height above the rough surface increases. The velocity-perturbation contours reveal an increase in the magnitude of the velocity perturbations by an order of magnitude by using the etched glass, which is directly caused by the increase in roughness height from HF etching. The ACL analyses also showed how the surface roughness produces small perturbation structures that merge and persist well into the midplane of the microchannel. Energy spectra analyses reveal a transfer of energy caused by the structures of the rough surfaces. Notably for the same Reynolds number, the etched surface produces velocity-perturbation structures that contain more energy and persist higher into the microchannel compared to the un-etched surface.

This research has shown that a chemical etching surface treatment and other stochastic rough surfaces, even at the nano-scale, have an effect on microfluidic flow that can be characterized and potentially be harnessed across a range of fluid flow rates. Devices that use microchannels such as lab-on-a-chip medical devices can therefore be tuned and optimized for their respective applications such as reagent mixing, bubble creation and transport, fluid transport, cell manipulation using stochastic surface roughness.

CHAPTER 1. GENERAL INTRODUCTION

Microchannels in Biomedical Devices

Microfluidics is a promising technology that is used extensively in biomedical devices, or so called “lab-on-a-chip” devices. These devices harness a network of microchannels to mix, react, and conduct fluid flow. The advantage of using lab-on-a-chip devices is their need for small amounts of reagents, portability (leading to point-of-care diagnostics), and increased speed of testing (Yager et al. (2006)). Figure 1 shows an example of a portable lab-on-a-chip device that is used to test blood for partial oxygen concentration, glucose, and lactate levels (Ahn et al. (2004)).

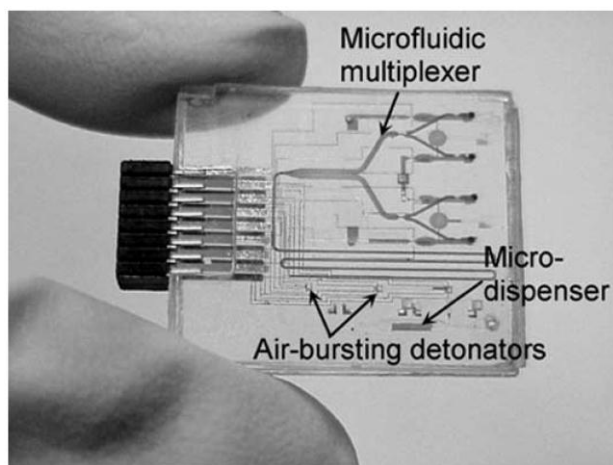


Figure 1. Example of lab-on-a-chip medical device by (Ahn et al. (2004))

The microfluid channel network is clearly seen throughout the chip, and the size of the chip relative to the human fingers holding it gives a visual understanding of how small and intricate these fluid systems are. In order to optimize the effectiveness of the lab-on-a-chip shown in Figure 1, or any other lab-on-a-chip using microfluidics, the flow characteristics within these channels should be known. Surface roughness within these microchannels may have a large effect on the fluid flow characteristics.

Research Motivation

Surface obstructions or surface roughness is typically used in order to advantageously disturb the microchannel fluid flow. The surface roughness of microchannels can be considered to fall into two distinct categories: inherent and deliberate. Most microchannel fabrication methods, such as wet and dry etching, produce a stochastic surface roughness with heights ranging in the nano- to micro- scale (Rodriguez et al. (2003)) similar to that pictured in Figure 2(b). This stochastic surface roughness is inherent to the etching process itself. Therefore, all microchannels created by these methods possess nano- to micro- scale stochastic surface roughness unless further processed to remove this inherent roughness.

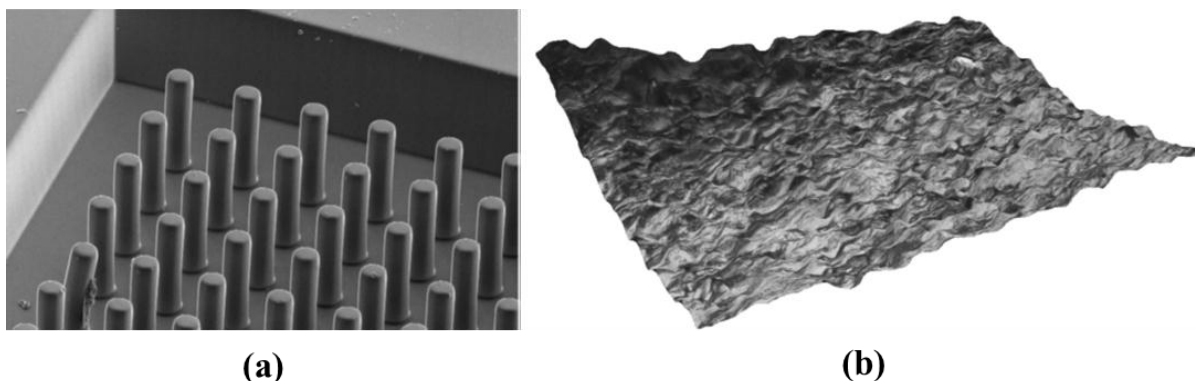


Figure 2. Examples of (a) deliberate roughness (McUsic et al. (2012)) and (b) stochastic roughness (Young et al. (2011)) on experimental microchannel surfaces.

Deliberate roughness, on the other hand, usually consists of micro-sized obstructions in the shape of cubes, pyramids, spheres, and others with consciously designed geometric dimensions as seen in Figure 2(a). They are deliberately designed and microfabricated onto the surface of the microchannel wall(s) to affect the fluid flow in a desired way. The deliberate surface roughnesses are usually ordered and periodic where obstructions may be placed in a grid fashion. In this thesis, a surface roughness is deliberately made to effect the fluid flow, however, it is characterized to be *stochastic* in nature, not ordered. The surface in this thesis study is created by using hydrofluoric-acid (HF) to etch into an originally smooth glass surface. The surface roughness characteristics (root-mean-squared height, height

distribution, or autocorrelation length) can be tailored according to the HF etching time and concentration (Ren et al. (2011)). In addition, the HF etching method is a simple, more cost-effective approach to creating microchannels and roughness on the microchannel surfaces to affect the fluid flow (Bahadorimehr et al. (2010)).

Characterization of how the flow is affected by the HF etched, stochastic surface has not been studied before using three-dimensional computational fluid dynamics (CFD), or more specifically, direct numerical simulations (DNS) that take advantage of high-powered parallel computing. *The main motivation of this thesis is to characterize the effect of the HF-etched surface roughness on microfluidic flow.* The novel aspect of this research revolves around the use of genuine surface topography in the computational domain, which has not been done before to this level of detail. A detailed description of how the rough surface was constructed for both experiments and simulations is found in the Appendix.

Thesis Organization

Chapters 2 and 3 correspond to the research goals outlined above. Specifically, Chapter 2 details the research done using micro-PIV experiments and DNS simulations for a Newtonian fluid (water), which forms a basis for experimental validation. Chapter 3 is research done only using DNS simulations for a Newtonian fluid (water) with a larger computational domain as compared to Chapter 2.

Chapter 3 also has a more extensive literature review of previous research done on the effect of surface roughness in microfluidic flow. Finally, Chapter 4 summarizes all of the conclusions drawn from the thesis and plans for future work in non-Newtonian fluid flow. References for each chapter's contents are given at the end of the individual chapters. Appendix A gives a more detailed description of the rough surface creation than the single journal papers provide. Appendix B gives the autocorrelation functions associated with data from Chapter 3.

References

- Ahn, C.H., Choi, J.W., Beaucage, G., Nevin, J.H., Lee, J.B., Puntambekar, A. & Lee, J. (2004) Disposable Smart Lab on a Chip for Point-of-Care Clinical Diagnostics. *Proceedings of the IEEE*. **92** No. 1. 154-173.
- Bahadorimehr, A.R., Yunas, J., Yeop Majlis, B. Low cost fabrication of microfluidic microchannels for Lab-On-a-Chip applications. *Electronic Devices, Systems and Applications (ICEDSA), 2010 Intl Conf.* pp.242-244, **11-14** April 2010.
- McUSIC, A.C., Lamba, D.A. & Reh, T.A. (2012) Guiding the morphogenesis of dissociated newborn mouse retinal cells and hES cell-derived retinal cells by soft lithography-patterned microchannel PLGA scaffolds. *Biomaterials*. **33**, 1396-1405.
- Ren, J., Ganapathysubramanian, B. & Sundararajan, S. (2011) Experimental analysis of the surface roughness evolution of etched glass for micro/nanofluidic devices. *J. Micromech. Microeng.* **21**, 025012.
- Rodriguez, I., Cpicar-Mihalic, P., Kuyper, C., Fiorini, G. & Chiu, D. (2003) Rapid prototyping of glass microchannels. *Analytica Chimica Acta*. **496**, 205-215.
- Yager, P., Edwards, T., Fu, E., Helton, K., Nelson, K., Tam, M. & Weigl, B. (2006) Microfluidic diagnostic technologies for global public health. *Nature*. **442**, 412-418.
- Young, P.L., Brackbill, T.P. & Kandlikar, S.G. (2011) Comparison of roughness parameters for various microchannel surfaces in single-phase flow applications. *Heat Transfer Engineering*. **30** (1-2), 78-90.

CHAPTER 2. NANO-SCALE SURFACE ROUGHNESS AFFECTS LOW RE FLOW: EXPERIMENTS AND MODELING

Modified from a paper to be submitted to *Applied Physics Letters*

R. Jaeger², J. Ren, Y. Xie, M. G. Olsen, S. Sundararajan, B. Ganapathysubramanian^{1*}

Abstract

Most micro-channel fabrication strategies generate nano- to micro- scale, stochastic surface roughness. This inherent stochasticity can potentially be harnessed to enhance microfluidic operations. This work investigates the effect of stochastic nanoscale roughness on low to moderate Reynolds number (0.06-6.5) Newtonian flow using concurrent modeling and experiments. We fabricate a microscopic channel with tailored hydrofluoric-acid-etched rough surfaces. Optical profilometry and micro-particle-image-velocimetry are used to characterize the surface roughness and resulting flow field in pressure-driven flow. These roughness and flow data are used in conjunction with an experimentally validated, very-large-scale Direct Numerical Simulation (~ 50 million unknowns) that resolves the effects of nanoscale roughness. Results from velocity contours and velocity-perturbation autocorrelations indicate that the nanoscale roughness causes flow perturbations that extend up to the mid-plane of the microchannel. For diffusion-dominated flows, this effect is insensitive to flow-rates. We observe a dependence of flow feature variability on changing surface roughness (via varying the HF-etching time).

Introduction

Soft lithography using SU-8 photoresist and poly(dimethylsiloxane) (PDMS) is a commonly used technique to fabricate microchannels. This method in conjunction with

¹ Department of Mechanical Engineering, Iowa State University, Ames, IA 50010

² Primary researcher and author

*To whom correspondence should be addressed. E-mail: baskarg@iastate.edu

hydrofluoric acid (HF) etching is an effective rapid prototype microfabrication process of microchannels [8,9,10]. A byproduct of HF etching is an inherent, stochastic surface roughness [11]. The surface roughness can exhibit variations in root-mean-squared roughness from microns to nanometers. This roughness has the potential to affect the fluid flow within the microchannel, especially the flow near the rough surface. Understanding the flow characteristics of fluids in microchannels with respect to their relative surface roughness (γ) is important for optimizing the effectiveness of microfluidic operations and has been the focus of recent studies [12,13,14]. The effect of *micro-scale surface roughness* ($\gamma = 1.6\%$) was examined [19] experimentally by using micro-PIV and comparing with a *smooth* computational fluid dynamics (CFD) simulation of a channel of the same geometry. Flow effects in relation *to periodic micro-scale obstructions* in height have also been investigated using CFD by various authors [20, 21, 22]. These analyses usually focus on periodic roughness and are invariably limited to 2D [23, 24, 26, 27]. In one study, Valdes et. al [25] used pyramidal shapes in a 3-dimensional domain that were randomly placed throughout the channel surface in accordance to data acquired from an actual surface. *However, the CFD surface did not mimic the actual surface exactly.* Instead, relative roughness and peak density values were acquired from the actual surface to generate the CFD surface. As a result, the true effect of a tangible surface was not investigated. Recently, Liu et.al [23] analyzed three-dimensional surface roughness using molecular dynamics in nanochannels with $\gamma = 3\%$, and found that random roughness had a greater effect on flow than periodic obstructions. While molecular dynamics simulations are exceedingly useful in gaining insight into the mechanics involved, they are limited to very small domains and time-scales due to their prohibitive computational cost.

We focus on two key issues that have not been addressed by previous investigations on roughness effects: We directly model realistic surface roughness that is extracted using optical profilometry. This is made possible by using high resolution DNS analysis (that is validated using concurrent micro-PIV experiments) which allows us to link nano-scale roughness to far-field flow features. We also focus on flows at low Reynolds number where

viscous forces dominate, which is common for microfluidic devices, and extensively characterize the effect of varying surface roughness.

Experimental Setup: Fabrication, characterization, and visualization

The experimental microchannel in this study was fabricated using PDMS and glass. The PDMS part was a replica made from an SU-8 mold and serves as three walls of the microchannel. The PDMS part and a glass substrate (slide) were then oxygen-plasma bonded together, creating a completely enclosed microchannel for fluid transport, with the glass forming the fourth (bottom) wall of the channel. We implemented hydrofluoric acid (HF) etching to create a surface roughness on the glass substrate that is reproducible and characterizable as a function of etching time [11]. A desired stochastic surface roughness can be fabricated according to the etching time and solution concentration [11].

In this study, we used an un-etched glass and a roughened glass obtained as follows. A glass slide (25 mm × 75 mm, Erie Scientific Company, Portsmouth, NH) was etched in buffered HF (6:1 volume ratio of 40% NH₄F in water to 49% HF in water; etch rate calibrated to 72 nm/min) for 30 minutes and immediately rinsed in deionized water for 5 minutes. After rinsing, the etched-glass slide was dried using nitrogen gas before being oxygen-plasma bonded to the PDMS replica. Etching time was limited below 40 minutes since longer etching times compromised the glass transparency necessary for micro-PIV measurements. The 30-minute etched glass is referred to simply as "etched glass" from here onward.

The microchannel's surface topography was obtained using a 3D Optical Surface Profiler (NewView™ 7100, Zygo Corporation, Middlefield, CT). The optical profilometer provided a scan area of 470 μm x 350 μm, with a lateral resolution of 0.73 μm and spatial resolution of 0.1 nm. The surface data obtained by the optical profilometer was directly used to model the surface roughness on the bottom surface of the CFD microchannel at the same spatial resolution.

In our experiments, micro-PIV visualization of microfluidic flow is possible with a microscopic imaging system that visualizes a small area within the microchannel. In the

micro-PIV experiment, the working fluid, deionized water, was seeded with 1 μm diameter Nile-red fluorescent carboxylate-modified microspheres (FluoSpheres, Invitrogen Corporation) as flow-tracing particles at a concentration of 0.04%. The seed particles were illuminated using a double-pulsed Nd:YAG laser. Images of the illuminated tracing particles were captured using a CCD camera. A 40x 0.6 NA objective lens paired with a 0.45x coupling, resulted in a total magnification of 18X and a depth of correlation of 7.8 μm [28]. Further details of the micro-PIV system can be found in Li and Olsen [29]. The overlapped area of adjacent interrogation windows was 50% resulting in an in-plane velocity vector species of 2 μm . In total, 1500 micro-PIV image pairs were captured at each depth and analyzed using the sum-of-correlation algorithm [30,31,32] to obtain the velocity field.

The surface data obtained by the optical profilometer is used to model the surface roughness on the bottom surface of the CFD microchannel at the same spatial resolution. This ensures that the surface roughness used for CFD simulations was experimentally derived and non-periodic. Figure 3 shows the computational domain. The trapezoidal shape of the CFD microchannel has identical dimensions as the micro-PIV experimental microchannel. The length of the channel is 350 μm (this is more than 10 times the surface roughness autocorrelation length (12.9 μm for the etched surface)). The grid is composed of 12.3 million hexahedral elements. The elements are concentrated near the walls to accurately capture the effect of the surface roughness and boundary layers. The clustering of hexahedral elements was greater near the rough surface.

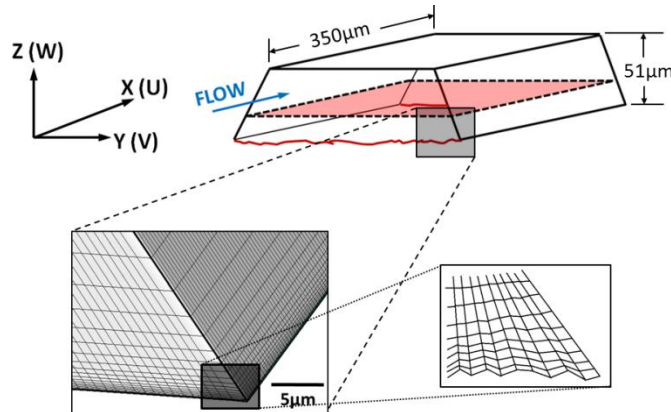


Figure 3. The geometry and mesh detail of the computational microchannel domain. The roughness height on the zoomed-in section is exaggerated for clarity. The width of the channel is 460 μm at the rough surface.

Modeling Framework: Mesh generation and solution technique

The full Navier-Stokes equations are solved assuming incompressible flow and constant fluid temperature. We utilize a highly scalable implementation of an incompressible flow solver using the Finite Element Method that incorporates Streamline-upwind/Petrov-Galerkin (SUPG) [33] and pressure-stabilizing/Petrov-Galerkin (PSPG) [34] terms for numerical stabilization. The applicability of the Navier-Stokes equation (validity of the continuum hypothesis) is ensured due to the fact that the Knudson number calculated on the smallest element (2.7×10^{-4}) is less than 10^{-2} [35]. We apply no-slip boundary conditions on the walls. Zhu et al. [36] showed that for a microchannel (with hydrophilic surfaces) with a hydraulic diameter larger than 30 μm , the no-slip boundary condition is valid. In addition to PDMS being hydrophilic, the etched glass is also hydrophilic [38] (A 29.5° contact angle of water on the etched-glass was measured to further verify hydrophilicity). The channel walls (PDMS and glass) are treated with an oxygen-plasma treatment, which has been shown to increase surface hydrophilicity [37]. Potential micro-sized air bubbles will also have no effect on slip. Micro-sized air bubbles have been known to create an effective slip at the wall by forming an immiscible fluid layer where the slip increases. However, if the capillary pressure is great enough to force the air out of the surface features, then the no-slip boundary condition is again valid, as proven by Barrat and Bocquest [39]. The minimum pressure

required to force fluid into a parallel slit of width h is: $P_o = \frac{2(\gamma_{LS} - \gamma_{SV})}{h}$ which is smaller than the pressure gradient applied in these experiments. A pressure drop boundary condition between inlet and outlet is maintained. The pressure drop is set to match the experimentally determined flow rate using the Hagen-Poiseuille flow equation, $\Delta P = \frac{128\mu L Q}{\pi D^4}$, where L is the length of the channel, μ is the dynamic viscosity, Q is the volumetric flow rate, and D is the hydraulic diameter. We analyzed cases using flow rates of 0.001 mL/min, 0.01 mL/min, 0.1 mL/min which corresponds to a Reynolds number of 0.065, 0.65, and 6.5, respectively.

Results and Discussion

The effect of surface roughness is investigated by looking at the fluid structures that evolve from the rough surface. We focus on fluid structures consisting of velocity perturbations caused by the roughness itself. In order to characterize these velocity perturbations, we use autocorrelation analysis, energy spectrum analysis, and visual analysis. By examining the fluid structure characteristics as a function of height from the rough surface, a zone of influence from the rough surface is established.

$$C(\tau) = \lim_{R \rightarrow \infty} \frac{2\pi}{R^2 \sigma^2} \int_0^R [h(r) - m][h(r + \tau) - m] dr$$

$$C(\tau) = \exp\left(\frac{-\tau}{\beta^*}\right)$$

The autocorrelation function, $C(\tau)$ is estimated for a velocity field in a plane to find β^* , the autocorrelation length. The autocorrelation length is defined as the lag distance where the autocorrelation function decays to $1/e$. Autocorrelation analysis is performed on velocity fields as slices in the xy -plane, highlighted in red in Figure 3, at increasing heights from the rough surface, in order to extract the influence of surface roughness as a function of height. Note that the autocorrelation is calculated using the velocity-component deviations from ideal flow (perturbations). The interrogation region was taken toward the center of the

microchannel away from the side-walls and entrance/exit to eliminate the side-wall boundary layer and boundary condition effects. The ACL of the v-velocity perturbations is used for validation between experiments and computational results.

Figure 4 shows the ACL as a function of height from the rough surface for computational results as well as experimental data. The uncertainty bars for the experimental data represent one standard deviation from the mean value. The experimental ACL was taken at 25.5 μm from the rough. The relationship and value of ACL between etched and unetched surfaces is consistent between computations and experiments. Table 1 summarizes the ACL values between experiments and CFD at 25.5 μm above the rough surface for etched and unetched surfaces.

Table 1. Comparison of experimental and DNS metrics at 25 μm from rough surface [μm].

Flowrate [ml/min]	Surface Type	ACL		Energy Spectra Slope Ratio	
		Exp.	DNS	Exp.	DNS
0.1 (Re = 6.5)	Etched	17.4 \pm 1.7	17.3 \pm 0.6	1.73 \pm 0.04	1.82 \pm 0.03
	Unetched	14.2 \pm 3.4	15.0 \pm 2.7		
0.01 (Re = 0.65)	Etched	16.7 \pm 1.6	17.5 \pm 1.2	2.86 \pm 0.17	2.15 \pm 0.04
	Unetched	16.8 \pm 1.4	15.0 \pm 2.9		

If the roughness effect on the fluid did not persist above the surface, then the ACL values would tend toward zero. However, the ACL starts small and increases to a constant value. This suggests that the effect from the surface roughness persists in the flow well above the rough surface. The coherent structures (eddies) start small near the rough surface and combine with increasing height from the rough surface. Figure 4 shows that the ACL as a function of height from the rough surface is very consistent across flow rates. Notice that while the ACL is insensitive to flow rate for these diffusion-dominated flows, it is sensitive to the roughness characteristic of the surface.

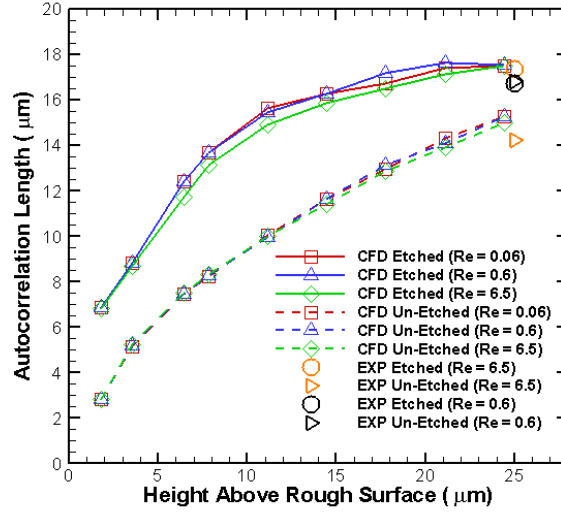


Figure 4. Autocorrelation lengths (ACL) of experimental and CFD v-velocity-component perturbations for both etched and un-etched surfaces at all flow rates, Q [ml/min].

While the autocorrelation length gives valuable information about the fluid structures, an energy spectra analysis can reveal the energy cascading effects of the surface roughness. Energy spectra analysis has been used successfully for velocity field analysis in a variety of fluid phenomena [41]. The energy spectrum is denoted as $E(k)$, where \hat{u} is the discrete Fourier transform of the velocity field [42] on a structured mesh with $n \times m$ points, where $\bar{E}(k) = \frac{1}{2} |\hat{u}(k, t)|^2$.

$$\hat{u}(k_x, k_y, t) = \frac{1}{\sqrt{mn}} \sum_{j_1=0}^{m-1} \sum_{j_2=0}^{n-1} u(x, y, t) e^{-i \left(\frac{j_1 k_x}{m} + \frac{j_2 k_y}{n} \right)}$$

$$E(k) = \sum_{k-\Delta k \leq k \leq k+\Delta k} \bar{E}(k_x, k_y)$$

Figure 5 shows the energy spectra of the total velocity perturbations. Figure 5a reveals that the energy cascade across wavelengths has a very similar structure throughout the spectrum of flow rates over etched glass, again supporting the notion of insensitivity of

effect of surface roughness as a function of flow rate. Clearly, the energy spectra in Figure 5b reveal that larger amounts of energy in the form of velocity perturbations are produced by etched glass. Also, Figure 5b shows that the energy produced by etched glass persists higher into the microchannel compared to unetched glass. There is a greater decay in the energy for unetched glass as the height from the rough surface increases, whereas the energy from the etched glass tends to persist. This is clearly seen in the slope of the energy spectra. For the etched and unetched surfaces this is approximately -4.75 and -8.64 , respectively. Not only is the perturbation energy larger for etched glass, but the larger slope for etched glass compared to unetched glass means there is a greater transfer of energy for etched glass [43]. Table 1 also compares the energy spectra slope ratios between experiments and simulations. The ratio is defined as the energy spectra of unetched/etched surfaces, and the numerical results agree with the experimental results within 5% for the higher flow rate.

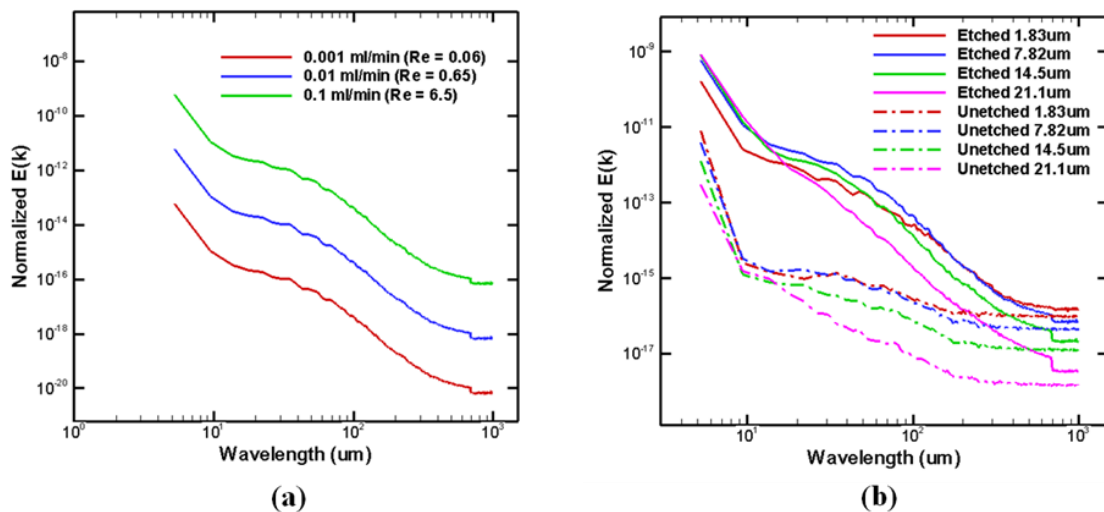


Figure 5. Energy spectra analysis of u-v-w velocity perturbation sum of squares: energy spectra of the velocity field as a function of flow rate (a) at $7.82\mu\text{m}$ above the rough surface of etched glass, and the energy spectra (b) of $Re = 6.5$ of etched and un-etched

We finally utilize visual representation of the velocity to investigate the fluid structure away from the surface by plotting velocity contours in the xz -plane. Note the dramatic effects due to roughness as seen in Figure 6(a-d) which shows the v -velocity

contours for both unetched and etched glass at multiple flow rates. There are large velocity plumes that originate from the rough surface and erupt well above the mid-plane of the microchannel. The R_{rms} of the etched glass (~ 19 nm) is slightly more than an order of magnitude greater than the un-etched glass (~ 1 nm), and not surprisingly, there is an order of magnitude increase in the velocity fluctuations between the etched and unetched surfaces. What is interesting is that the small perturbations originating from the rough surface seem to combine and merge into larger structures as the height from the surface increases. These combinations give rise to the velocity plumes seen in Figure 6.

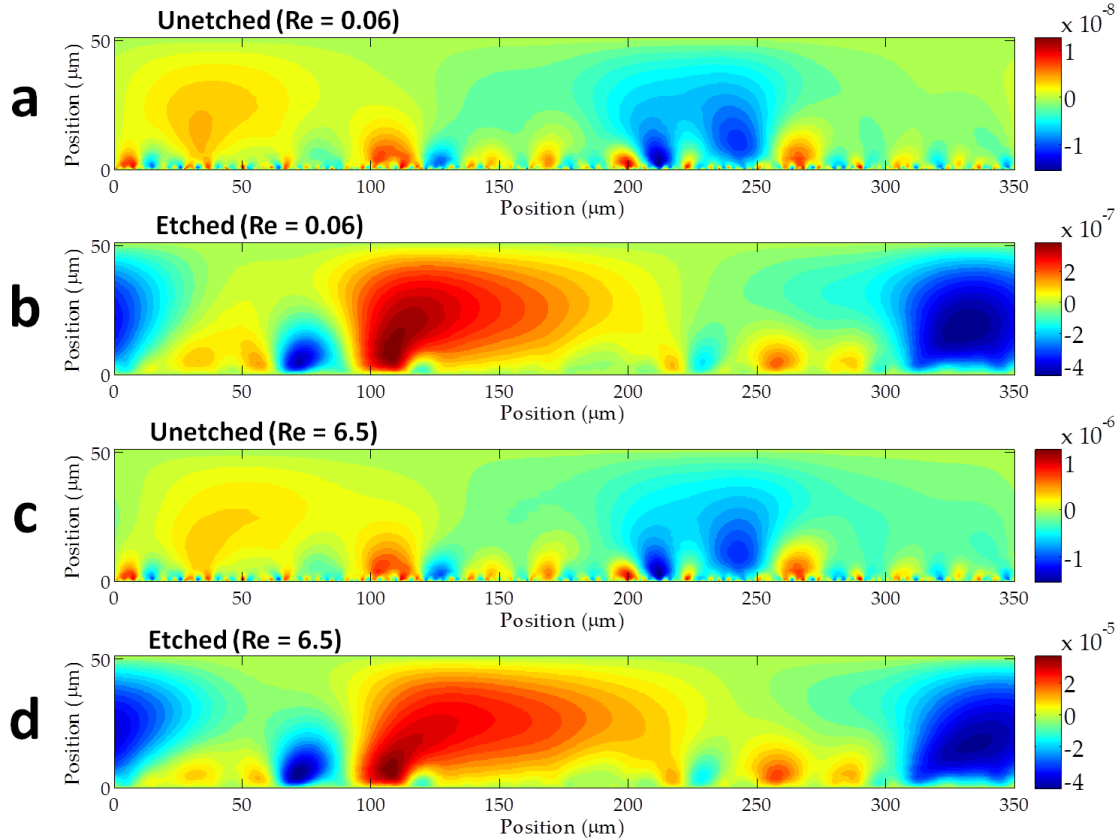


Figure 6. V-velocity component contour plots of (a) Re = 0.06 un-etched, (b) Re = 0.06 etched, (c) Re = 6.5 un-etched, and (d) Re = 6.5 etched (fluid flow goes from left to right). The xz-plane slices were taken $175\mu\text{m}$ away from the microchannel side wall.

Conclusions and Outlook

We have shown that the effect of stochastic nano-scale surface roughness on microfluidic flow can be studied using computational fluid dynamic DNS simulations. Additionally, we have shown that validation between micro-PIV experiments and a large DNS simulation is possible using autocorrelation and energy spectra. CFD analysis lends to a deeper understanding of the characterization of the fluid flow within the microchannel, and the highly resolved DNS simulations reveal the flow to be characterizable. We show that for a range of flow rates that are diffusion dominated, the energy transfer is consistently characterizable. Autocorrelation and velocity contour analyses showed that the nano-scale surface roughness produced small structures that combine and persist well above the rough surface. In addition, the energy spectra analyses show the small eddies produced by the etched surface give rise to higher energy eddies that decay more slowly than eddies produced by the unetched surface.

The chemical etching surface treatment and other stochastic rough surfaces, even at the nano-scale, can be characterized and potentially be harnessed across a range of fluid flow rates. Devices that use microchannels such as lab-on-a-chip medical devices can potentially be tuned and further optimized for their respective applications such as reagent mixing, bubble creation and transport, fluid transport, cell manipulation by leveraging the effects of stochastic surface roughness.

References

1. Yager, P., Edwards, T., Fu, E., Helton, K. , Nelson, K., Tam, M. & Weigl, B. (2006) Microfluidic diagnostic technologies for global public health. *Nature* 442, 412–418.
2. Crowley, T. & Pizziconi, V. (2005) Isolation of plasma from whole blood using planar microfilters for lab-on-a-chip applications. *Lab On A Chip*, 5, 922--929.

3. Sollier, E., Rostaing, H., Pouteau, P., Fouillet, Y. & Achard, J. (1996) Passive microfluidic devices for plasma extraction from whole human blood. *Sensors and Actuators B* 141, 617–624.
4. VanDellinder, V. & Groisman, A. (2006) Separation of plasma from whole human blood in a continuous cross-flow in a molded microfluidic device. *Anal. Chem.* 78, 3765–3771.
5. Cho, Y., Lee, J., Park, J., Lee, B., Lee, Y. & Ko, C. (2007) One-step pathogen specific DNA extraction from whole blood on a centrifugal microfluidic device. *Lab On A Chip* 7, 565–573.
6. Jeon, N., Baskaran, H., Dertinger, S., Whitesides, G. , Van De Water, L. & Toner, M. (2002) Neutrophil chemotaxis in linear and complex gradients of interleukin-8 formed in a microfabricated device. *Nature Biotechnology* 20, 826–830.
7. Chen, X., Cui, D., Liu, C., Li, H. & Chen, J. (2007) Continuous flow microfluidic device for cell separation, cell lysis and DNA purification. *Analytica Chimica Acta.* 584, 237–243.
8. Rodriguez, I., Cpicar-Mihalic, P., Kuyper, C., Fiorini, G. & Chiu, D. (2003) Rapid prototyping of glass microchannels. *Analytica Chimica Acta* 496, 205–215.
9. Kolli, M., Hamidouche, M., Bouaouadja, N. & Fantozzi, G. (2009) HF etching effect on sandblasted soda-lime glass properties. *J. of the European Ceramic Society* 29, 2697–2704.
10. Muscat, A., Thorsness, A. & Montano-Miranda, G. (2001) Characterization of residues formed by anhydrous hydrogen fluoride etching of doped oxides. *J. Vac. Sci. Technol. A.* 19, 1854–1861.
11. J. Ren, B. Ganapathysubramanian, S. Sundararajan (2011) Experimental analysis of the surface roughness evolution of etched glass for micro/nanofluidic devices, *Journal of Micromechanics and Microengineering*, 21 025012.
12. Hosokawa, K., Fujii, T., & Endo, I. (1999) Handling of Picoliter Liquid Samples in a Poly(dimethylsiloxane)-Based Microfluidic Device. *Anal. Chem.* 71 (20), 4781-4785.
13. Londe, G., Chunder, A., Wesser, A., Zhai, L., & Cho, H.J. (2008) Microfluidic valves based on superhydrophobic nanostructures and switchable thermosensitive surface for lab-on-a-chip (LOC) systems. *Sensors and Actuators B: Chemical.* 132 (2), 431-438.

14. Gunther, A., Khan, S., Thalmann M., Trachsel, F., & Jensen, K. (2004) Transport and reaction in microscale segmented gas-liquid flow. *Lab on a chip*, 4, 278-286.
15. Santiago, J.G., Wereley, S.T., Meinhart, C.D., Beebe, D.J., & Adrian, R.J. (1998) A particle image velocimetry system for microfluidics. *Experiments in Fluids*, 25: 316-319.
16. Meinhart, C.D., Wereley, S.T., & Santiago, J.G. (1998) PIV measurements of microchannel flow. *Experiments in Fluids*, 27: 414-419.
17. Fujisawa, N., Nakamura, Y., Matsuura, F., & Sato, Y. (2006) Pressure field evaluation in microchannel junction flows through a μ PIV measurement. *Microfluidics and Nanofluidics*, 2: 447-453.
18. Liu, Y., Olsen, M.G., & Fox, R.O. (2009) Turbulence in a microscale confined impinging jets reactor. *Lab on a Chip*, 9:1110-1118.
19. Silva, G., Leal, N. & Semiao, V. (2008) Micro-PIV and CFD characterization of flow in a microchannel: velocity profiles, surface roughness and poiseuille numbers. *International J. of Heat and Fluid Flow* 29, 1211–1220.
20. Rawool, A. S., Mitra, S.K., & Kandlikar, S. G. (2005) Numerical simulation o flow through microchannels with design roughness. *Microfluid Nanofluid* DOI 10.1007/s10404-005-0064-5.
21. Jeon, W. & Shin, C. B. (2009) Design and simulation of passive mixing in microfluidic systems with geometric variations. *Chemical Engineering Journal* 152, 575-582.
22. Koo, J. & Kleinstruer, C. (2003) Liquid flow in microchannels: experimental observations and computational analyses of microfluidics effects. *Journal of Micromechanics and Microengineering* 13, 568-579.
23. Liu, J., Wang, M., Chen, S. & Robbins, M. (2010) Molecular simulations of electroosmotic flows in rough nanochannels. *Journal of Computational Physics* 229, 7824–7847.
24. Valdes, J., Miana, M., Pelegay, J.L., Nunez, J.L. & Putz, T. (2007) Numerical investigation of the influence of roughness on the laminar incompressible fluid flow through annular microchannels. *International Journal of Heat and Mass Transfer* 50, 1865–1878.
25. Valdes, J., Miana, M., Martinez, M., Gracia, L. & Putz, T. (2008) Introduction of a length correlation factor for the calculation of laminar flow through microchannels

- with high surface roughness. *International Journal of Heat and Mass Transfer* 51, 4573–4582.
26. Xiong, R. (2010) Fluid Flow in Trapezoidal Silicon Microchannels With 3D Random Rough Bottoms. *Journal of Fluids Engineering* 133, 031102-1–031102-7.
 27. Xiong, R. & Chung, J.N. (2010) A new model for three-dimensional random roughness effect on friction factor and heat transfer in microtubes. *International Journal of Heat and Mass Transfer* 53, 3284–3291.
 28. Bourdon, C.J., M.G. Olsen, and A.D. Gorby, The depth of correlation in micro-PIV for high numerical aperture and immersion objectives. *Journal of Fluids Engineering-Transactions of the ASME*, 2006. 128(4): p. 883-886.
 29. Li, H. & Olsen, M.G. (2006) Micro PIV measurements of turbulent flow in square microchannels with hydraulic diameters from 200 μm to 640 μm . *International Journal of Heat and Fluid Flow*, 27:123-134.
 30. Meinhart, C.D., Wereley, S.T., & Santiago, J.G. (2000) A PIV algorithm for estimation, time-average velocity fields. *Journal of Fluids Engineering*, 122:285-289.
 31. Olsen, M.G., & Adrian, R.J. (2000) Out-of-focus effect on particle image visibility and correlation in microscopic particle image velocimetry. *Experiments in Fluids*, 29:S166-S174.
 32. Bourdon, C.J., Olsen, M.G., & Gorby, A.D. (2004) Validation of an analytical solution for depth of correlation in microscopic particle image velocimetry. *Measurement Science and Technology*, 15:318-327.
 33. Hughes, T. & Brooks, A. (1979) A multidimensional upwind scheme with no crosswind diffusion. *Finite Element Methods for Convection Dominated Flows* (ed. Hughes T.J.R.) ASME New York, Wiley.
 34. Tesduyar, T.E., Mittal, S., Ray, S.E. & Shih, R. (1991) Incompressible flow computations with stabilized bilinear and linear equal-order-interpolation velocity-pressure elements. *Computer Methods in Applied Mechanics and Engineering* 95, 221-242.
 35. Gad-el-Hak, M. (1999) The fluid mechanics of microdevices-the freeman scholar lecture. *Trans. ASME J: J. Fluids Engineering* 121, 5-33.

36. Zhu, L., Tretheway, D., Petzold, L. & Meinhart, C. (2005) Simulation of fluid slip at 3D hydrophobic microchannel walls by the lattice Boltzmann method. *Journal of Computational Physics*. 202, 181–195.
37. Gulec, H., Sarioglu, K. & Mutlu, M. (2006) Modification of food contacting surfaces by plasma polymerisation technique. Part I: Determination of hydrophilicity, hydrophobicity and surface free energy by contact angle method. *Journal of Food Engineering*. 75, 187–195.
38. Sikalo, S., Marengo, M., Tropea, C. & Ganic, E.N. (2002) Analysis of impact of droplets on horizontal surfaces. *Experimental Thermal and Fluid Science*. 25, 503–510.
39. Barrat, J., & Bocquet, L. (1999) Large slip effect at nonwetting fluid-solid interface. *Physical Review Letters*. 82 No. 23, 4671-4674.
40. Zhang & Sundararajan (2005) The effect of autocorrelation length on the real area of contact and friction behavior of rough surfaces. *Journal of Applied Physics* 97, 103526-1—103526-7.
41. Singh S., & Mittal, S. (2004) Energy spectra of flow past a circular cylinder. *International Journal of Computational Fluid Dynamics*. 18, 671-679.
42. W.H. Press, S.A. Teukolsky, W.T. Vetterling, & B.P. Flannery, Numerical Recipes in C: The Art of Scientific Computing, Second Edition (New York: Cambridge University Press, 1992).
43. Kundu, P. K. & Cohen, I. M., Fluid Mechanics, Fourth Edition (Kidlington, Oxford: Elsevier Inc., 2008).

CHAPTER 3. INVESTIGATING THE EFFECT OF NANO-SCALE SURFACE ROUGHNESS ON MICROFLUIDIC NEWTONIAN FLUID FLOW

Modified from a paper to be submitted to the *Journal of Fluid Mechanics*. Future work will extend this paper to non-Newtonian fluid flow (shear thinning).

R. Jaeger², Y. Xie, M. G. Olsen, S. Sundararajan, B. Ganapathysubramanian^{1*}

Abstract

Microfluidics is becoming increasingly exploited in lab-on-a-chip medical testing devices. The principal element of microfluidic devices consists of a microchannel network to mix, react, and conduct fluid flow. Microchannels are commonly produced by poly(dimethylsiloxane) PDMS molding, soft lithography, and wet chemical etching. Hydrofluoric-acid (HF) etching of microchannels has been shown experimentally to generate nano-scale, stochastic surface roughness. This roughness can play a critical role for flow characterization in order to optimize medical testing processes within microchannels. In this study, a computational fluid dynamics (CFD) analysis is performed with a three-dimensional microchannel for low Reynolds number ($Re < 10$), pressure-driven flow. The CFD microchannel has the first experimentally-derived surface roughness. Velocity-component perturbation contours, energy spectra, and autocorrelation length at heights above the rough surface are analyzed. Each flow characterization method revealed that small eddies produced at the rough surface merge and form larger eddies as height above the rough surface increased. The energy created by the etched surface produced velocity perturbations an order of magnitude larger than the un-etched surface and persisted higher into the microchannel above the etched surface. Velocity-component perturbation contours, energy spectra, and

¹ Department of Mechanical Engineering, Iowa State University, Ames, IA 50010

² Primary researcher and author

*To whom correspondence should be addressed. E-mail: baskarg@iastate.edu

autocorrelation length proved to be valuable ways to characterize the fluid flow and potentially harness the effects from stochastic surface roughness in microfluidic flow.

Introduction

Medical-testing devices that take advantage of microfluidic concepts are becoming ever more relevant because of their ease-of-use, size, use of small amount of reagents, and potentially low cost. For example, in Yager et al. (2006), microfluidic medical devices have been proven to allow precise volumes of fluid to be measured and processed efficiently without the need for an expert laboratory technician. As a result, expensive and cumbersome clinical laboratories become unnecessary and medical care can be brought to underdeveloped regions. The applications for medical devices that use microchannels are widespread. For instance, so called “lab-on-a-chip” devices for blood testing and blood manipulation are seen in Crowley & Pizziconi (2005), Sollier et al. (2009), and VanDellinder & Groisman (2006). These devices utilize microchannels in different ways to separate plasma from whole blood. Another example is DNA extraction from whole blood by utilizing centrifugal microfluidics in Cho et al. (2007). Cancer research has also been advanced with the use of microchannel medical devices in Jeon et al. (2002). In this instance, low Reynolds number flows in microchannels generate detectable gradients of chemotactic factors to be observed in real time. Figure 7 illustrates an example of a microchannel segment used in a medical device developed by Chen et al. (2003) to advance research in point-of-care genetic analysis. Additionally, point-of-care blood testing for E.coli has been advanced by RoyChaudhuri et al. (2011) using a microfluidic device, thereby reducing the reagent quantity and volume of blood needed for testing compared to traditional laboratory methods that do not exploit microfluidics.

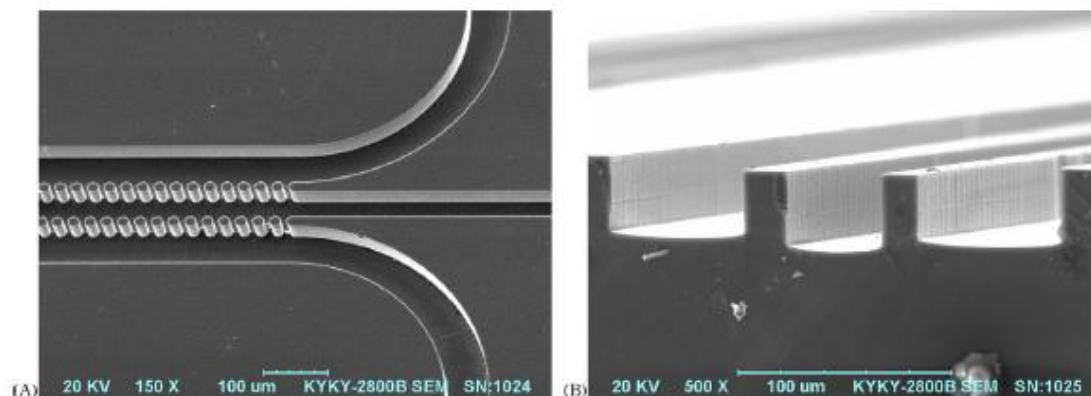


Figure 7. Example microchannel in medical device by Chen et al. (2003)

The microchannels in Sollier et al.(2009) and most medical devices are produced by an inexpensive technique known as soft lithography using SU-8 photoresist and poly(dimethylsiloxane) (PDMS). Rapid prototype production of microchannels using these methods in conjunction with hydrofluoric (HF) acid etching has been proven effective by Rodriguez et al. (2003), Kolli et al. (2009), and Muscat et al. (2001), which reduces the cost of fabrication. A byproduct of HF-acid etching is an inherent, stochastic surface roughness (Ren et al. (2011)). The surface roughness can vary from nano-scale heights to micro-scale heights and has the possibility to affect the fluid flow within the microchannel, especially the flow near the rough surface. Understanding the flow characteristics of fluids in etched microchannels is important for optimizing the effectiveness of the medical testing processes. This understanding can result in potential mechanisms to harness effect from the surface roughness's stochastic nature.

One way to understand the effect of surface roughness on fluid flow in microchannels is based on experimentally measuring bulk flow properties such as Poiseuille (Po) number or the friction factor. The experimental characterization of flow by measuring friction factor and Po number in microchannels has been investigated by many groups, including Pfund et al. (2000), Judy et al. (2002), and Celata et al. (2006), but the effect of surface roughness was not a main focus in these studies. Friction factor and Po number measurements have been performed with specific attention to microchannel surface roughness by Phares et al. (2005) and Hrnjak & Tu (2003). Phares et al. (2005) observed a qualitative deviation in drag

coefficient between smooth stainless steel tubes and rough polyimide tubes with relative roughness of 3.4%. Relative roughness, ε , can be generally defined as the ratio of the root-mean-squared surface-roughness height to hydraulic diameter. Hrnjak & Tu (2003) studied the effect of surface roughness for laminar and turbulent flow. For $Re = 3000$ and $\varepsilon = 0.14\%$, the friction factor increased 30% beyond the expected value from the Churchill equation in turbulent flow. However, the effect of roughness in laminar flow was small enough to be overcome by experimental measurement uncertainty. From the experiments by Hrnjak & Tu (2003), it is demonstrated that small, stochastic roughness can induce energy into the flow. However, a difficulty of bulk measurements and experimental analysis of roughness in general is defining an exact hydraulic diameter to base friction factor measurements on, which causes a decrease in bulk measurement confidence. The above sources demonstrate a clear effect on flow from surface roughness, but bulk-flow measurements give little or no detail on the structure of the flow within the microchannel. Other methods are better suited for visualizing flow characteristics in microchannels.

An alternate experimental flow characterization method is micro particle image velocimetry (micro-PIV) in which particle laden flow is illuminated in order to reveal a velocity flow field. Experimental design for micro-PIV from Devasenathipathy et al. (2003) allowed the possibility of micron-resolution data for microfluidic flows. Unlike bulk-flow measurements, micro-PIV measurements can produce spatial and temporal velocity data within the flow. Micro-PIV then allows visualization of streamwise or transverse velocity profiles within a *transparent* microchannel. The effect of random micro-scale surface roughness ($\varepsilon = 1.6\%$) was examined by Silva et al. (2008) experimentally by using micro-PIV, and the effect of roughness was made evident by direct comparison to a smooth computational fluid dynamics (CFD) channel of the same geometry. By constructing velocity profiles throughout the microchannel, Silva et al. (2008) reported Po numbers that differed by 11% between the experimental microchannel with surface roughness and an ideally smooth CFD channel, thereby revealing a considerable effect due to a relatively small surface roughness. A limiting factor of micro-PIV is the depth of correlation (Olsen & Adrian (2000) and Bourdon et al. (2004)), which is usually on the order of $5\mu\text{m}$ or more depending on the

experimental equipment and setup. Therefore, velocity-field perturbations $5\mu\text{m}$ or closer to the surface are hidden and impossible to resolve with confidence.

The work done by Silva et al. (2008) demonstrates the importance of considering the effect of random surface roughness and the value that CFD can play with respect to surface roughness examination. There is little to no research using CFD on real stochastic surface roughness, but two-dimensional and periodic surfaces have been investigated. Flow effects in relation to periodic, ordered micro-scale obstructions in height have also been investigated using CFD in a two-dimensional domain by Rawool et al. (2006) and Gamrat et al. (2008), where the relative roughnesses were $\varepsilon = 0.5\%$ and $\varepsilon = 0.4\%$, respectively. Here, the obstructions were on the order of $10\mu\text{m}$, and it was found that as obstruction height increases, the friction factor increases nonlinearly for the tested flow regime (from $\text{Re} = 100$ to $\text{Re} = 2000$). Conical shaped, period surface roughness was explored by Croce et al. (2007) with $\varepsilon = 2.65\%$. For $\text{Re} = 100$ -1500, the roughness produced a 16% difference in Po number as compared to an ideally smooth CFD channel. From the literature, low Reynolds number, diffusion-based flow below $\text{Re} = 50$ has not been greatly considered, which is common at such small length scales in microfluidic lab-on-a-chip devices. Also, the above mentioned work is focused on periodic roughness, but stochastic roughness is more representative of genuine, inherent microchannel surfaces.

Random surface roughness was examined using CFD by Valdes et al. (2007), Valdes et al. (2008), Xiong (2010), Liu et al. (2010), and Xiong & Chung (2010). A two-dimensional domain with $\varepsilon = 0.6\%$ created by Valdes et al. (2007) showed an increase in Po number of 8.8% as compared to a smooth channel with the same geometry. This helps establish the significance of small, random surface roughness on microfluidic flow. In later studies, Valdes et al. (2008) used pyramidal shapes in a 3-dimensional domain that were randomly placed throughout the channel surface in accordance to data acquired from an experimental surface under study. However, the CFD surface did not mimic the experimental surface exactly. Instead, relative roughness and peak density values were acquired from the actual surface in order to generate the CFD surface. As a result, the true effect of a genuine stochastic, engineered surface was not investigated. Liu et al. (2010) also conducted work

with three-dimensional surface roughness using molecular dynamics in nanochannels with $\epsilon = 3\%$, and found that random roughness had a greater effect on flow than periodic obstructions with the same mean height. Xiong (2010) also generated random roughness in a three-dimensional microchannel, but the relative roughness ranged from 1.66-5.39%, well above the value of etched glass. In this case of Xiong & Chung (2010), the roughness was obtained using a Gaussian distribution. In actuality, surface roughness heights are not merely randomly generated heights distributed on a surface, neither are they periodic in nature. Genuine surface roughness is stochastic, and it obeys an important spatial parameter known as autocorrelation. Ren et al. (2011) describes the relationship between surface height and autocorrelation of stochastic surface roughness, specifically HF-etched glass. As a result, genuine microchannel surfaces need to be reconstructed for CFD surfaces in order to obtain similar effects from surface roughness inherent to fabricated microchannels that use chemical etching as applied in lab-on-a-chip devices.

Overall, micro-PIV has been proven to be an effective method for experimental microchannel flow visualization, but it is not particularly useful for capturing near-wall velocity perturbations. Furthermore, CFD analysis of microfluidic flow is able to resolve the small perturbations that emanate from the surfaces of the microchannel walls. However, there have been deficiencies in the analyses of the effect of roughness in microchannel fluid flow. One of these deficiencies is flow at low Reynolds number, which is common for microfluidic devices at such small length scales. Additionally, genuine nano-scale surface roughnesses have not been directly modeled using CFD. Therefore, characterization of microfluidic flow within microchannels with nano-scale surface roughness remains incomplete.

Surface roughness affecting the flow in the previously mentioned studies is typically ordered, periodic micrometer sized obstructions. These orderly obstructions have costly manufacturing procedures. In our experiment, we use hydrofluoric acid (HF) etching to create a stochastic, nano-scale surface roughness that is repeatable and characterizable as a function of etching time. The desired stochastic surface characteristics can be tailored according to HF acid concentrations and etching times. Etching by HF acid may serve as a very cost effective method to manufacture roughness that effects flow. The effect that this

etched stochastic roughness has on microfluidic flow is studied in this paper by comparing etched glass to smooth, un-etched glass.

Our contributions are to quantify the effects of stochastic nano-scale surface roughness ($\varepsilon < 0.022\%$) on the flow characteristics of a Newtonian at low Reynolds number in microfluidic channels by utilizing an *experimentally-driven computational approach*. The first large scale three-dimensional microchannel with experimentally derived, random nano-scale surface roughness is modeled using computational fluid dynamics, more specifically, highly resolved direct numerical simulations (DNS). The resulting velocity field is then analyzed using velocity contours, energy spectra, and autocorrelation length to characterize the flow effect.

Computational Domain Construction

In order to investigate the impact of nano-scale surface roughness on fluid flow through microchannels, a three-dimensional CFD microchannel domain was created that uses an experimentally-derived rough surface as the bottom wall. The other three walls of the microchannel are modeled as ideally smooth surfaces. Figure 8 depicts a view of the microchannel with the CFD mesh shown near the rough surface. The experimentally-derived methods used to create the rough surface are outlined below.

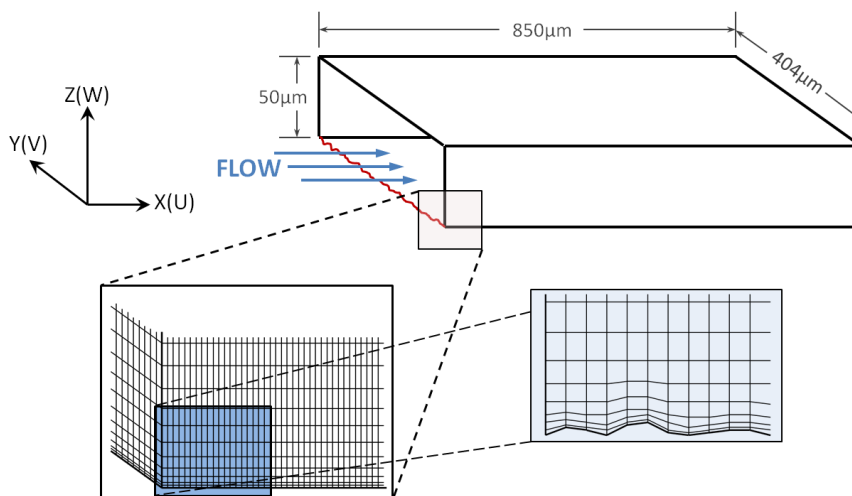


Figure 8. Computational microchannel domain geometry with mesh details.

Microchannel Roughness: Experimental Manufacturing

Microchannels for fluid transport are typically processed using molding techniques, and surface roughness is always prevalent to some degree. The computational microchannel in this study was modeled according to a typical microchannel manufacturing process using a soft lithography technique with SU-8 photoresist and PDMS. A masked is applied over the SU-8 with a pattern of the intended microchannel. Then, the SU-8 is exposed to UV light. The UV-exposed SU-8 photoresist cures and is used to serve as the mold for the final microchannel. Liquid PDMS is poured over the SU-8 and allowed to cure. The cured PDMS replica is peeled off the mold and now serves as three walls of the microchannel. A glass slide (etched or un-etched) is then oxygen-plasma bonded to the PDMS replica to form the bottom surface of the channel, thereby creating a completely enclosed rectangular microchannel for fluid transport. The process outlined above is typical in manufacturing microchannels with the addition of an etched glass surface.

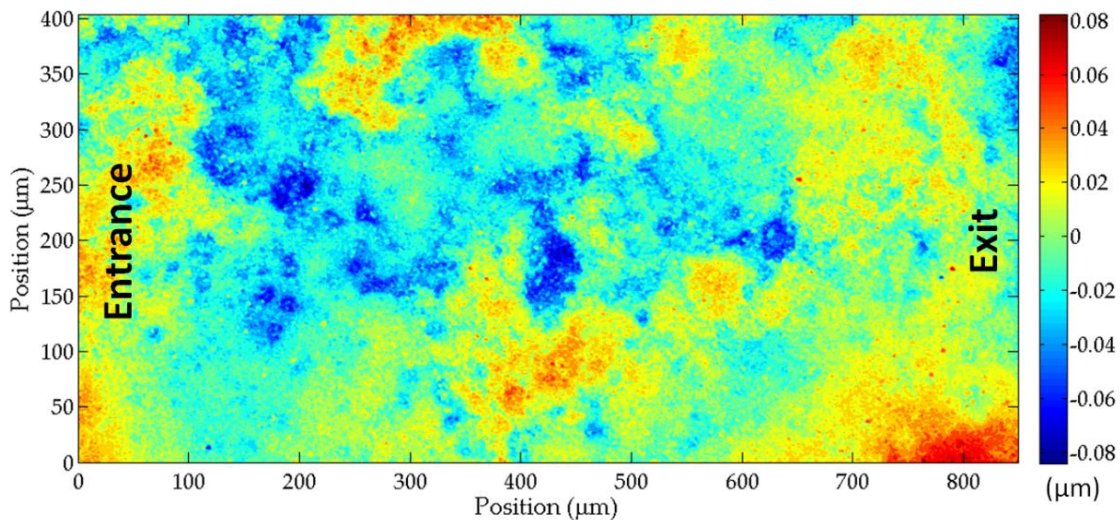


Figure 9. Height contours [μm] of the etched surface used in the computational domain.

Wet HF acid etching of the glass slide was used to create the rough surface under study within the microchannel. First, the glass slide ($25 \text{ mm} \times 75 \text{ mm}$, Erie Scientific

Company, Portsmouth, NH) was etched in buffered HF acid (6:1 volume ratio of 40% NH₄F in water to 49% HF acid in water; the etch rate was found to be 72nm/min) for 30 minutes and immediately rinsed in deionized water for 5 minutes. After rinsing, the etched-glass slide was dried using nitrogen gas before being oxygen-plasma bonded to the PDMS replica. The 30-minute etched glass is referred to simply as "etched glass" from here onward, and the virgin glass is referred to as "un-etched glass". Etched and un-etched glass are directly compared to each other as smooth and rough surfaces in this study.

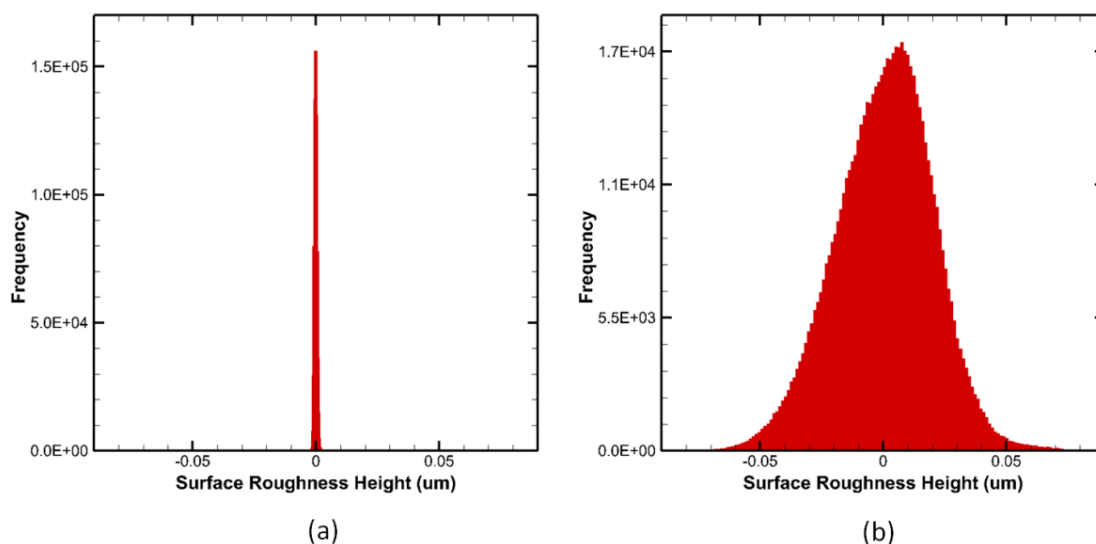


Figure 10. Histogram of the surface heights for (a) un-etched and (b) etched surfaces.

The experimental microchannel's surface topography was obtained using a 3D Optical Surface Profiler (NewView™ 7100, Zygo Corporation, Middlefield, CT). The optical profilometer provided single scan areas of 460μm x 350μm, with a lateral resolution of 0.71μm and height resolution of 0.1nm. Side-by-side profilometer scans of the surface were taken and stitched together to form a continuous surface of the dimensions in Figure 8. This surface data obtained by the optical profilometer for both etched and un-etched glass was directly used to model the surface roughness on the bottom surface of the CFD microchannel at the same spatial resolution. Hence, the surface roughness used for CFD simulations was experimentally derived and non-periodic. Height contours of the etched glass surface used in

the computational microchannel are shown in Figure 9. The un-etched surface was created in a similar manner with optical profilometer scans of un-etched glass.

Microchannel Roughness: Characterization

As discussed in Introduction, there has been a large investigation of periodic or deterministic roughness, and the attributes of periodic roughness are easy to characterize. However, the surface roughness in this study produced by etching, or any stochastic process, is not periodic and more difficult to characterize sufficiently. There are many descriptors for a stochastic surface roughness, but descriptors that are most relevant to this study are: histograms, root-mean-squared (RMS) roughness height, and the autocorrelation length (ACL). Also, relative roughness is used to characterize the roughness with respect to the microchannel's hydraulic diameter.

The un-etched and etched glass RMS height (z_{RMS}) was found to be 1.0nm and 19.8nm, respectively. To find the relative roughness (ϵ), the RMS height and hydraulic diameter ($D_H = 89\mu\text{m}$) of the microchannel are used, defined in equations (2) and (1), respectively, where A is the cross-sectional area of the microchannel, and P is the wetted perimeter. Since the entire channel is filled with fluid, the wetted perimeter is simply the entire perimeter of the rectangular microchannel. The relative roughness was found to be $\epsilon = 0.001\%$ and $\epsilon = 0.022\%$ for un-etched and etched surfaces, respectively, which is an order of magnitude lower than previous studies performed in the literature review.

$$D_H = \frac{4A}{P} \quad (1)$$

$$z_{RMS} = \sqrt{\frac{1}{n} \sum_{i=1}^n z_i^2} \quad (2)$$

$$\epsilon = \frac{z_{RMS}}{D_H} * 100\% \quad (3)$$

The histograms in Figure 10 show the height distributions of the surface roughness on the bottom surface of the microchannel for both etched and un-etched glass. The autocorrelation length is determined from the autocorrelation function, which is a cross-correlation of a waveform with itself. In this case, the waveform is spatially dependent surface roughness. It is defined in equations (4) and (5) for spatially varying surface roughness (Zhang & Sundararajan (2005)).

$$C(\tau) = \lim_{R \rightarrow \infty} \frac{2\pi}{R^2 \sigma^2} \int_0^R [h(r) - m][h(r + \tau) - m] dr \quad (4)$$

$$C(\tau) = \exp\left(\frac{-\tau}{\beta^*}\right) \quad (5)$$

The ACL for rough surfaces, and most engineering surfaces, is equal to β^* . The ACL is defined as the lag distance at which the value of the autocorrelation function, $C(\tau)$, is $1/e$. The autocorrelation function is assumed to be isotropic to obtain a single ACL value. The ACL for the un-etched and etched surfaces used in the CFD simulations was $0.94\mu\text{m}$ and $10.6\mu\text{m}$, respectively. The effects from these stochastic surfaces are ensured to be fully encompassing of the surface characteristics since the microchannel length is $850\mu\text{m}$, which is more than 80 times longer than the ACL of each surface.

Governing Equations: Newtonian Fluid

For the fluid analyses, we assume a Newtonian fluid with constant properties, incompressible, steady state, and laminar flow. Conservation of mass and momentum are represented by equations (6) and (7), respectively, in Einstein-tensor notation.

$$\frac{\partial u_i}{\partial x_i} = 0 \quad (6)$$

$$u_j \frac{\partial u_i}{\partial x_j} = -\frac{1}{\rho} \frac{\partial p}{\partial x_i} + \nu \left(\frac{\partial^2 u_i}{\partial x_j^2} \right) \quad (7)$$

Where u_i is the velocity component in the i direction, p is the pressure, ρ is the fluid density, and ν is the kinematic viscosity.

Validity of Continuum Hypothesis

The mass and momentum conservation equations require that the continuum hypothesis is valid throughout the computational domain. The continuum hypothesis is valid in fluid flow if the Knudson number (Kn) is less than 10^{-2} (Gad-el-Hak (1999)). The Knudson number is calculated by equation (8) where \mathcal{L} is the mean-free path of the fluid in question and L is the characteristic length. It is defined as the ratio of the mean-free path of the fluid molecule to a length scale. We define the characteristic length to be the smallest line segment connecting two nodes of the CFD grid, which is $0.106\mu\text{m}$. The mean-free path of a water molecule is 0.2\AA (Kirby (2010)). Consequently, Kn is 1.887×10^{-4} and affirms the validity of the continuum hypothesis by two orders of magnitude.

$$Kn = \frac{\mathcal{L}}{L} \quad (8)$$

Another approach is to consider the number of water molecules occupying the smallest grid cell volume. The smallest cell volume in the CFD grid was $0.0534\mu\text{m}^3$. The volume of one molecule of water is approximately 30\AA^3 (Gnanendran & Amin (2004), Iguchi et al. (2009), and Sasaki et al. (1996)). Therefore, the number of water molecules in the smallest grid cell is 1.78×10^9 . This large number of molecules confirms the use of continuum modeling.

Validity of No-Slip Boundary Condition

A no-slip boundary condition at solid walls for macroscopic fluid flow through channels is well accepted. However, the no-slip boundary condition is not a guaranteed condition for micro- and nano-sized fluid channels. Zhu et al. (2005) used micro-PIV experimental results and lattice-Boltzmann simulations to independently obtain the no-slip boundary condition for hydrophilic wall surfaces. It has been shown by Zhu et al. (2005) that

for a microchannel with a hydraulic diameter larger than $30\mu\text{m}$ whose surfaces are hydrophilic, then the no-slip boundary condition is valid. The hydraulic diameter in this study is $89\mu\text{m}$, clearly large than $30\mu\text{m}$.

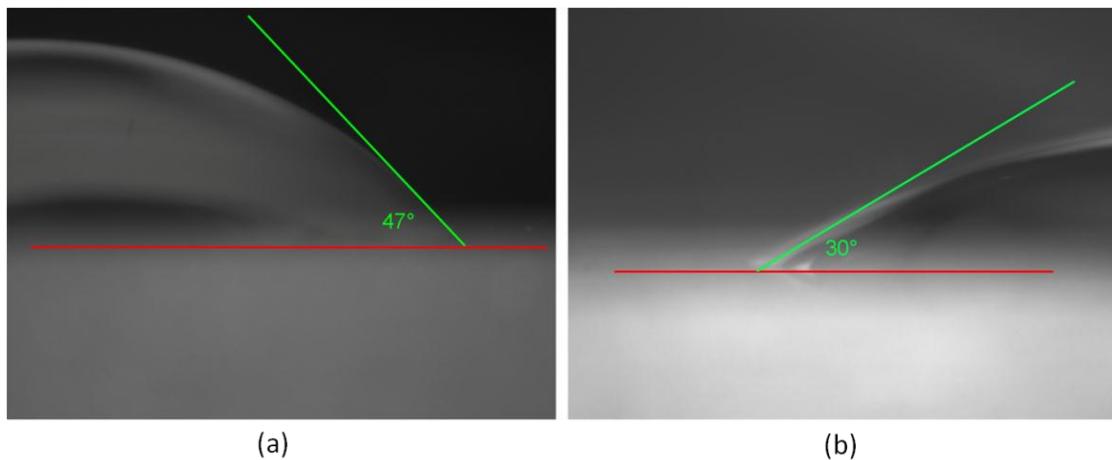


Figure 11. Measured contact angles of water on un-etched glass (a) and etched glass (b). The contact angles prove they are both hydrophilic surfaces.

Typically, microchannels constructed with PDMS are treated with an oxygen-plasma treatment, which increases the surface hydrophilicity as described by Gulec et al. (2006). The etched glass used in this study for etched and un-etched glass is confirmed to be hydrophilic from studies by Sikalo et al. (2002) and from contact angle measurements in Figure 11. All microchannel surfaces used in the experimentally derived microchannel are therefore hydrophilic. In order to match this quality, a no-slip boundary condition was applied to the microchannel walls of the CFD simulations.

The no-slip boundary condition used can also be related to the mean free path of water. The mean free path of water, 0.2\AA , is small relative to the characteristic size of the flow, the hydraulic diameter. Therefore, the water molecules near the wall exchange tangential momentum with the rough wall more than they exchange tangential momentum with the bulk fluid. The tangential velocity is thereby well approximated to be zero near the wall (Kirby (2010)).

Computational Methods

CFD Microchannel Grid

Figure 8 shows the computational domain where the fluid is being investigated. The grid is composed of 28 million hexahedron-type elements. The elements are concentrated near the walls (and more so near the rough wall) to accurately capture the effect of the surface roughness and boundary layers. The geometric ratio was limited to 1.1 for elements near the rough surface and 1.3 for elements farther from the rough surface.

Flow Rate Determination

The determination of a flow rate to be tested was based on a sampling of microfluidic devices used in the literature (Ali et al. (2003), Liu et al. (2004), and Petersson et al. (2005)). The microfluidic devices applied a range of flow rates for multiple applications including lipid separation and DNA hybridization/amplification. From the literature, flow rates of $Q = 0.001\text{-}0.1\text{ml/min}$ were chosen for this study. The flow can be characterized a diffusion-dominated laminar flow by the very low Reynolds number defined by equation (9).

$$Re = \frac{\rho V D_H}{\mu} \quad (9)$$

Where the hydraulic diameter, D_H , is the characteristic length, V is the mean velocity of the fluid, and μ is the dynamic viscosity of the fluid. The Reynolds number was determined using constant fluid properties of water given in Table 2. The flow rates in this study of $Q = 0.001, 0.01, \text{ and } 0.1\text{ml/min}$ correspond to Reynolds numbers of $Re = 0.06, 0.6, \text{ and } 6.5$, respectively.

Table 2. Fluid properties of water used in CFD simulation

Operating temperature (isothermal) [°C]	20
Density, ρ [kg/m ³]	998.2
Dynamic viscosity, ν [kg/ms]	0.001002

Solution Framework

CyStorm, a high-performance parallel computing cluster at Iowa State University, enabled CFD simulations with a high number of grid elements and degrees of freedom. The Finite Element Method was employed to simulate the flow in the rough channel. For the concern of accuracy, the streamline-upwind/Petrov-Galerkin (SUPG) method (Hughes & Brooks (1979)), and the pressure-stabilizing/Petrov-Galerkin (PSPG) method (Tesduyar et al. (1991)) were used to stabilize the numerical results. SUPG/PSPG methods improve convergence for the incompressible-flow simulation by modifying the weighting function with stabilized terms based on local velocity and pressure fields. Weak formulations of Navier-Stokes equation can be written as shown in equation (10).

$$\int_{\Omega} \omega \cdot \left[(u \cdot \nabla)u + \nabla p - \frac{1}{Re} \nabla^2 u \right] d\Omega + \int_{\Omega} q \nabla \cdot u d\Omega + \sum_{e=1}^{n_{el}} (\delta + \epsilon) \cdot \left[(u \cdot \nabla)u + \nabla p - \frac{1}{Re} \nabla^2 u \right] = 0 \quad (10)$$

$$(u \cdot \nabla)u \rightarrow (u_{guess} \cdot \nabla)u \quad (11)$$

Where Ω is the physical domain, Ω^e is the finite element, ω is the Galerkin weighting function, δ and ϵ are SUPG and PSPG terms. The temporal terms do not appear because the flow is assumed to be stable in the channel because the Reynolds number is very low.

The Navier-Stokes equation is a non-linear equation, which cannot be solved directly using Finite Element Method. One option is using an iterative strategy for which a guessed value of velocity is used to transform the nonlinear convection term into a linear term, as seen in equation (11), where u_{guess} is a guessed, constant velocity field. Then, by solving this linear equation, a new velocity field can be obtained. The guessed velocity is replaced with

the new velocity field, and this procedure is repeated until the solution and the guessed value's maximum norm reaches 10^{-13} .

This method can guarantee the convergence, but the number of iterations becomes cumbersome because of the high fluctuation involved in the current problem. To increase the rate of convergence, we use the Newton-Raphson method to solve this nonlinear equation. For the current problem, denote the Navier-Stokes equation as a functional, $\mathcal{F}(u, p): [C_2(\Omega)]^2 \rightarrow \mathbb{R}$, of velocity function $u(x)$ and pressure function $p(x)$. The Navier-Stokes equation can then be written as $\mathcal{F}(u, p) = 0$. The general form of the Newton-Raphson scheme for the Navier-Stokes equation is seen in equation (12).

$$[u_{k+1}, p_{k+1}] = [u_k, p_k] - [\delta\mathcal{F}(u_k, p_k)]^{-1}\mathcal{F}(u_k, p_k) \quad (12)$$

Where $\delta\mathcal{F}(u_k, p_k)$ is the variation of \mathcal{F} with respect to u and p . An initial guess value of u and p is given, where $k=0,1,2,\dots$. Applying the stabilized Galerkin method on the above scheme, we get the weak form equation of δu and δp as shown in equation (13).

$$\begin{aligned} & \int_{\Omega} \omega \cdot \left[(\delta u \cdot \nabla)u + (u \cdot \nabla)\delta u + \nabla\delta p - \frac{1}{Re} \nabla^2 \delta u \right] d\Omega + \int_{\Omega} q \nabla \cdot \delta u \, d\Omega \\ & + \sum_{e=1}^{n_{el}} (\delta + \epsilon) \cdot \left[(\delta u \cdot \nabla)u + (u \cdot \nabla)\delta u + \nabla\delta p - \frac{1}{Re} \nabla^2 \delta u \right] \\ & = \int_{\Omega} \omega \cdot \left[(u \cdot \nabla)u + \nabla p - \frac{1}{Re} \nabla^2 u \right] d\Omega + \int_{\Omega} q \nabla \cdot u \, d\Omega \\ & + \sum_{e=1}^{n_{el}} (\delta + \epsilon) \cdot \left[(u \cdot \nabla)u + \nabla p - \frac{1}{Re} \nabla^2 u \right] = 0 \end{aligned} \quad (13)$$

Here, δu and δp are increments of u and p , which take the values of the solution at the previous step. The convergence of iterations is monitored by the 2-norm of the Navier-Stokes equation: $\|\mathcal{F}(u_k, p_k)\|_2$. When $\|\mathcal{F}(u_k, p_k)\|_2 < \epsilon$, where ϵ is a small positive number, the solution is accepted as the real solution field. For these simulations, we take $\epsilon = 1e-13$.

Periodic Boundary Conditions

The computational space needed to be minimized due to the high-resolution surface roughness topography. Consequently, a considerably long microchannel to achieve fully-developed flow could not be simulated. Instead, periodic boundary conditions were applied to the entrance and exit of the simulation domain to achieve fully-developed flow. Boundary conditions for the solution framework require the pressure drop to be known along the channel. We used the Hagen-Poiseuille flow, equation (14), to estimate an initial guess for the pressure drop in the microchannel. The pressure drop is then iterated to achieve the desired flow rate.

$$\Delta P = \frac{128\mu L Q}{\pi D_H^4} \quad (14)$$

Where ΔP is the pressure drop, L is the length of the channel, μ is the dynamic viscosity, Q is the volumetric flow rate, and D_H is the hydraulic diameter. ΔP increases linearly with Q for the constant viscosity case of a Newtonian fluid.

Results and Discussion

The effect of the un-etched and etched glass on microfluidic flow can be seen easily using velocity contours at certain planes within the microchannel. In all velocity visualization and analysis throughout this paper, the ideal flow has been subtracted from the flow field, thereby giving the component-wise velocity perturbations (u,v,w). Figure 12 shows the xz-plane of the microchannel at distance of 175 μ m away from the side wall in order to discount boundary effects from the side walls. Here, the contours of v-velocity perturbations are shown for etched and un-etched surfaces for the same Reynolds number.

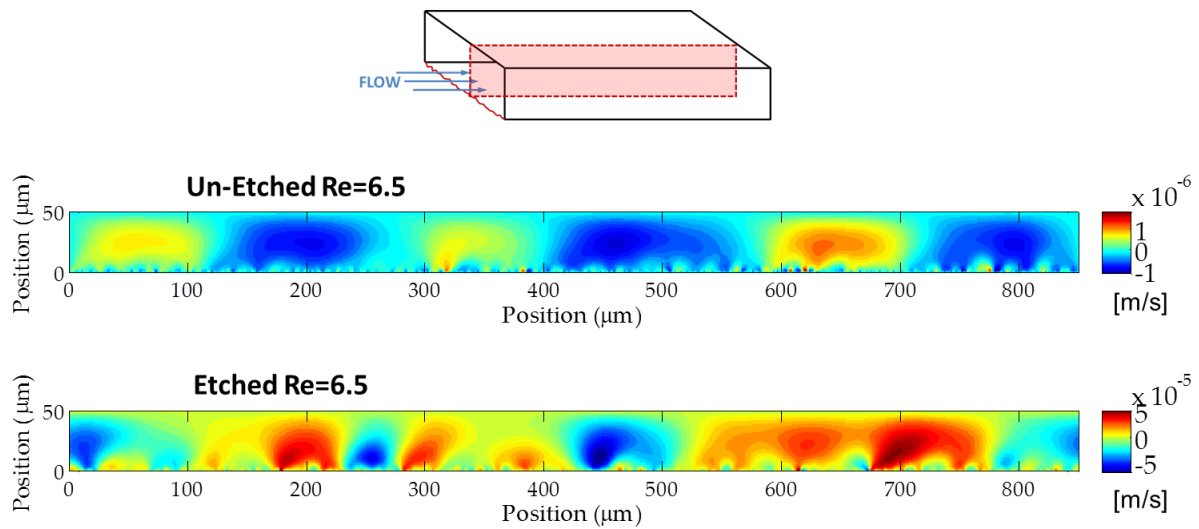


Figure 12. V-velocity contours in the xz -plane (depicted in the shaded red region above) of etched and un-etched glass surfaces for the same Reynolds number.

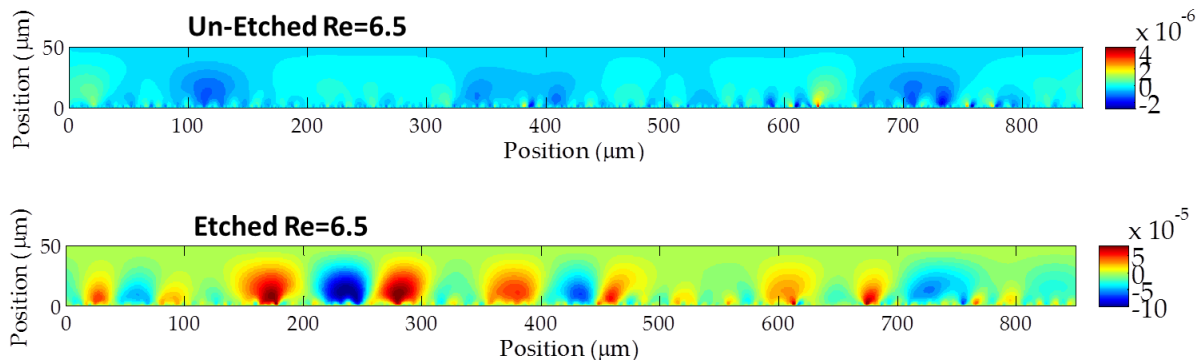


Figure 13. W-velocity contours in the xz -plane of etched and un-etched glass surfaces for the same Reynolds number.

The structures of the perturbations are clearly noticeable. These “structures” are regions of velocity perturbations that resemble plumes emanating from the bottom rough surface. Qualitatively, the structures are very small near the bottom surface for both etched and un-etched surfaces. The small structures combine as the height above the rough surface increases to form larger structures that affect the fluid flow more so than the smaller structures. The un-etched surface has less variability in the perturbations throughout the

plane as compared to the etched surface, which is a direct relation to the variability in the surface roughness as shown in the height histograms of Figure 10.

Quantitatively, Figure 12 shows an order of magnitude increase in the v-velocity perturbations for etched glass as compared to the un-etched glass surface. For diffusion based flows, this is a considerable increase since the RMS-heights for etched and un-etched glass are 1.0nm and 19.8nm, respectively, an order of magnitude increase.

Since many of the microfluidic devices operate in this diffusion-dominated flow regime, it is important to look at the full range of Reynolds numbers in this study. Figure 14 shows the v-velocity perturbation contours of the etched glass but for all Reynolds numbers: $Re = 6.5$, 0.6 , and 0.06 . The structure of the perturbations for $Re = 0.06$ and $Re = 0.6$ are virtually unchanged throughout. The only clear difference is their magnitude as a result of the Reynolds number. The structure for $Re = 6.5$ and $Re = 0.6$ are still similar, but the momentum of the fluid starts to affect the structures slightly in $Re = 6.5$. Within the diffusion-dominated flow regime, the velocity perturbation structures are insensitive to flow rate.

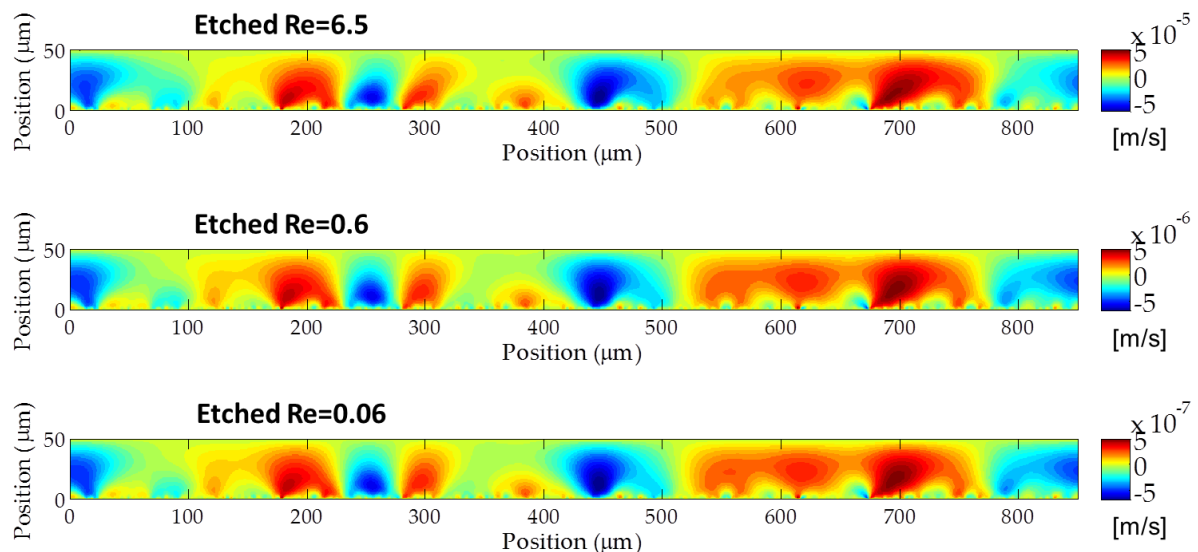


Figure 14. V-velocity contours in the xz-plane for an etched glass surface for all tested Reynolds numbers.

As mentioned in the Microchannel Roughness: Characterization section, an important descriptor of surface roughness is the autocorrelation length (ACL). The autocorrelation function and ACL was defined previously in equation (4) and equation (5), respectively, but it is now applied to the velocity perturbation field in the xy-plane instead of surface heights. The ACL gives a characteristic length of the velocity-perturbation structures discussed above. Figure 15 depicts the xy-plane and the ACL of both v- and w-velocity perturbations. The qualitative observations made from the velocity contours are now confirmed quantitatively by the ACL metric. Figure 15(a) shows the v-velocity perturbations ACL as a function of height above the rough surface for both etched and un-etched surfaces. The small perturbation structures that emanate from the rough surface correspond to a small ACL value. Similarly, the perturbation structures combine as height from the rough surface increases, which corresponds to the increase in ACL as the height above the rough surface increases. In both Figure 15(a) and Figure 15(b), the ACL increases and reaches a leveling point near the midplane of the microchannel. The leveling point suggests that the perturbations in the flow are persisting even as height increases from the rough surface into the midplane of the microchannel. This leveling point is true for both etched and un-etched surfaces.

The ACL analysis above characterized the perturbation structure size as a function of height from the rough surface, but the ACL does not give information about the strength of the perturbation or the energy contained in the perturbation structures. However, energy spectra analyses of the flow give a representation of the energy contained in the perturbations, emanating from the etched and un-etched rough surfaces. The sum of the squares of the u-, v-, and w-velocity perturbations are calculated and analyzed for the energy spectra, now referred to as the uvw-velocity perturbations.

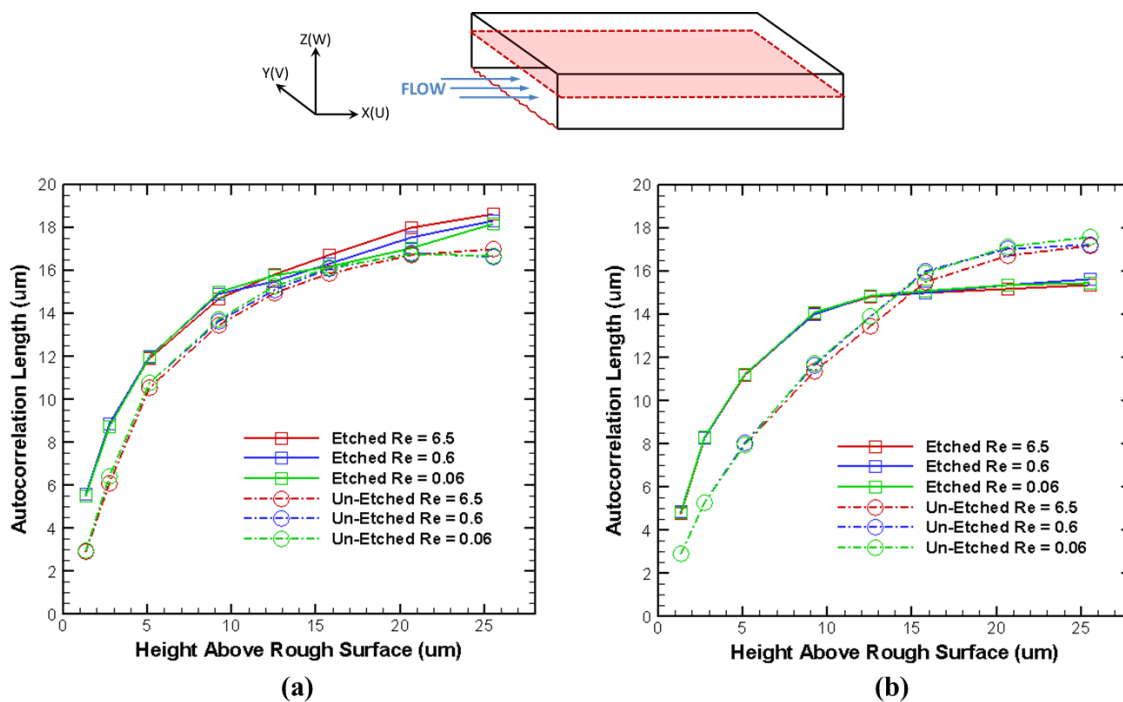


Figure 15. Autocorrelation length (ACL) as a function of height above the rough surface of the (a) v-velocity and (b) w-velocity perturbations in the xy-plane.

Energy spectra analyses have been used before in turbulent eddies of flow around a cylinder by Singh & Mittal (2004). The velocity energy spectra, $\bar{E}(k)$, is defined below in equations (15) and (16), where \hat{u} is the discrete Fourier transform of the velocity field Press (1992) on a structured mesh with $n \times m$ points, assuming the perturbation field is isotropic. The kinetic energy density is defined as $\bar{E}(k) = \frac{1}{2} |\hat{u}(k, t)|^2$.

$$\hat{u}(k_x, k_y, t) = \frac{1}{\sqrt{mn}} \sum_{j_1=0}^{m-1} \sum_{j_2=0}^{n-1} u(x, y, t) e^{-i\left(\frac{j_1 k_x}{m} + \frac{j_2 k_y}{n}\right)} \quad (15)$$

$$E(k) = \sum_{k-\Delta k \leq k \leq k+\Delta k} \bar{E}(k_x, k_y) \quad (16)$$

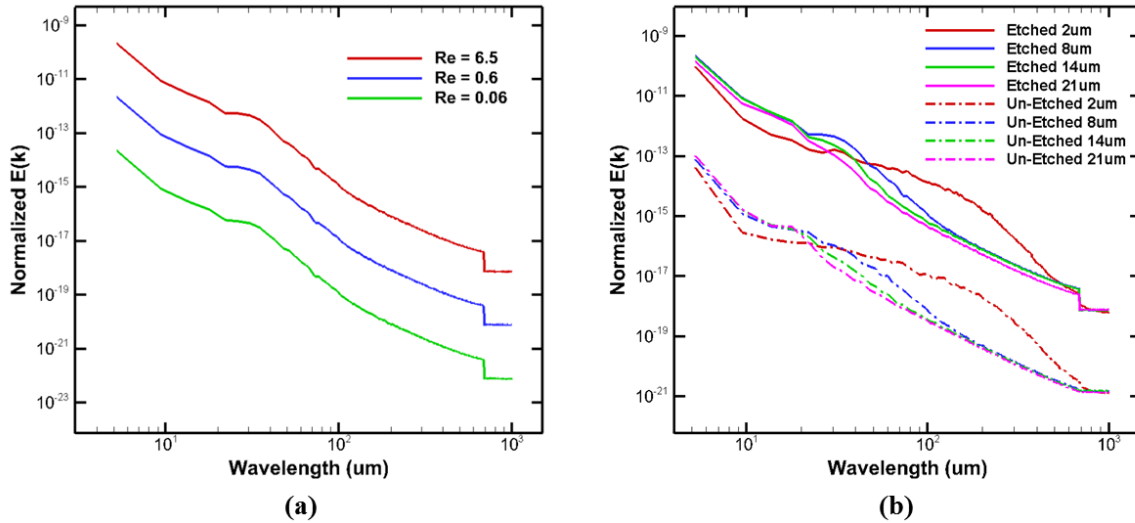


Figure 16. Energy spectra of (a) uvw-velocity perturbations as a function of Reynolds number $7\mu\text{m}$ above the rough surface and (b) the uvw-velocity perturbations in the xy-plane as a function of height above the rough surface.

Once again, the insensitivity of the effect due to roughness from Reynolds number is shown in Figure 16(a). The shape and trend of the energy spectra is practically the same for each Reynolds number. Figure 16(b) shows the energy spectra of the uvw-velocity perturbations with respect to etched and un-etched surfaces as a function of height above the rough surface. There is more than an order of magnitude increase in the energy created by the etched surface compared to the un-etched surface. Additionally, the energy cascade in the small-wavelength region ($< 10\mu\text{m}$) differs between etched and un-etched glass. The slope of the small-wavelength region is more negative for the un-etched glass compared to the etched glass, which reveals greater energy decay for un-etched glass compared to the etched glass rough surface.

Coming back to the ACL, the greater value for un-etched glass at the midplane of the microchannel in Figure 15(b) says that the characteristic length of the perturbations is larger. Yet, the energy spectra analyses reveal that larger structures with respect to ACL do not correlate to larger amounts of energy produced by the rough surface.

Conclusions

Overall, we have shown that an experimentally driven three-dimensional computational study for microfluidic surface roughness is possible. Additionally, we have shown that the stochastic nature of the surface roughness and its effect on fluid flow can be characterized with numerous tools including velocity-perturbation contours, autocorrelation length, and energy spectra analyses.

These different analyses illuminate the effect of the rough surface in different ways. Visually, the contours show that both the etched and un-etched rough surfaces produce very small velocity perturbation structures very near the rough surface that combine and form larger structures as the height above the rough surface increases. Also, the contours reveal the increase in the velocity perturbations by an order of magnitude, which is directly caused by the HF-acid surface etching. The ACL analyses also show how the surface roughness produces small perturbations that merge and persist well into the midplane of the microchannel. The energy spectra analyses again reveal a transfer of energy caused by the structures of the rough surfaces. Notably, the etched surface produces velocity structures that contain more energy and persist more at the same Reynolds number compared to the un-etched surface.

The process of wet HF-acid etching to produce a stochastic rough surface has proven to be an effective method of inducing energy into microchannel flow, especially under the diffusion dominated flow regime. Moreover, the flow structure's insensitivity to Reynolds number gives more applicability to characterization results across a range of flow rates. The flow and energy characterization methods used in this study can lead to more thorough comprehension and harnessing of the effect that stochastic roughness within microchannels has on many microfluidic devices, such as lab-on-a-chip medical devices.

References

- Ali, M., Kirby, R., Goodey, A., Rodriguez, M., Ellington, A., Neikirk, D. & McDevitt, J. (2003) DNA Hybridization and Discrimination of Single-Nucleotide Mismatches Using Chip-Based Microbead Arrays. *Analytical Chemistry*. **75**, 4732-4739.
- Bourdon, C.J., Olsen, M.G., & Gorby, A.D. (2004) Validation of an analytical solution for depth of correlation in microscopic particle image velocimetry. *Measurement Science and Technology*. **15**, 318-327.
- Celata, G.P., Cumo, M., McPhail, S. & Zummo, G. (2006) Characterization of fluid dynamic behaviour and channel wall effects in microtube. *International Journal of Heat and Fluid Flow*. **27**, 135-143.
- Chen, X., Cui, D., Liu, C., Li, H. & Chen, J. (2007) Continuous flow microfluidic device for cell separation, cell lysis and DNA purification. *Analytica Chimica Acta*. **584**, 237-243.
- Cho, Y., Lee, J., Park, J., Lee, B., Lee, Y. & Ko, C. (2007) One-step pathogen specific DNA extraction from whole blood on a centrifugal microfluidic device. *Lab On A Chip*. **7**, 565--573.
- Croce, G., D'agaro, P. & Nonino, C. (2007) Three-dimensional roughness effect on microchannel heat transfer and pressure drop. *International Journal of Heat and Mass Transfer* **50**, 5249-5259.
- Crowley, T. & Pizziconi, V. (2005) Isolation of plasma from whole blood using planar microfilters for lab-on-a-chip applications. *Lab On A Chip*. **5**, 922-929.
- Devasenathipathy, S., Santiago, J.G., Wereley, S.T., Meinhart, C.D. & Takehara, K. (2003) Particale imaging techniques for microfabricated fluidic systems. *Experiments in Fluids*. **34**, 504-514.
- Gad-el-Hak, M. (1999) The fluid mechanics of microdevices--the freeman scholar lecture. *Trans. ASME J: J. Fluids Engng*. **121**, 5-33.
- Gamrat, G., Favre-Marinet, M., Le Person, S., Baviere, R. & Ayela, F. (2008) An experimental study and modeling of roughness effects on laminar flow in microchannels. *J. Fluid Mech*. **594**, 339-423.
- Gnanendran, N. & Amin, R. (2004) Modeling hydrate formation kinetics of a hydrate promoter-water-natural gas system in a semi-batch spray reactor. *Chemical Engineering Science*. **59**, 3849-3863.

- Gulec, H., Sarioglu, K. & Mutlu, M. (2006) Modification of food contacting surfaces by plasma polymerisation technique. Part I: Determination of hydrophilicity, hydrophobicity and surface free energy by contact angle method. *Journal of Food Engineering*. **75**, 187-195.
- Hrnjak, P. & Tu, X. (2007) Single phase pressure drop in microchannels. *International Journal of Heat and Fluid Flow*. **28**, 2-14.
- Hughes, T. & Brooks, A. (1979) A multidimensional upwind scheme with no crosswind diffusion. *Finite Element Methods for Convection Dominated Flows* (ed. Hughes T.J.R.). ASME New York, Wiley.
- Iguchi, H., Takaishi, S., Takashi, K., Miyasaka, H., Yamashita, M., Matsuzaki, H. & Okamoto, H. (2009) Direct synthesis and crystal structure of dehydrated state in vapochromic MMX-type quasi-one-dimensional iodide-bridged platinum complexes. *J. Inorg. Organomet. Polym.* **19**, 85-90.
- Jeon, N., Baskaran, H., Dertinger, S., Whitesides, G., Van De Water, L. & Toner, M. (2002) Neutrophil chemotaxis in linear and complex gradients of interleukin-8 formed in a microfabricated device. *Nature Biotechnology*. **20**, 826-830.
- Judy, J., Maynes, D. & Webb, B.W. (2002) Characterization of frictional pressure drop for liquid flows through microchannels. *International Journal of Heat and Mass Transfer*. **45**, 3477-3489.
- Kirby, B. J. (2010) *Micro- and Nanoscale Fluid Mechanics*. New York: Cambridge University Press, 30-31.
- Kolli, M., Hamidouche, M., Bouaouadja, N. & Fantozzi, G. (2009) HF etching effect on sandblasted soda-lime glass properties. *J. of the European Ceramic Society*. **29**, 2697-2704.
- Liu, J., Wang, M., Chen, S. & Robbins, M. (2010) Molecular simulations of electroosmotic flows in rough nanochannels. *Journal of Computational Physics*. **229**, 7824-7847.
- Liu, R., Yang, J., Lenigk, R., Bonanno, J. & Grodzinski, P. (2004) Self-Contained, Fully Integrated Biochip for Sample Preparation, Polymerase Chain Reaction Amplification, and DNA Microarray Detection. *Analytical Chemistry*. **76**, 1824-1831.
- Muscat, A., Thorsness, A. & Montano-Miranda, G. (2001) Characterization of residues formed by anhydrous hydrogen fluoride etching of doped oxides. *J. Vac. Sci. Technol. A*. **19**, 1854-1861.

- Olsen, M. & Adrian, R. (2000) Out-of-focus effects on particle image visibility and correlation in microscopic particle image velocimetry. *Experiments in Fluids [Suppl. 1]*. **29**, S166-S174.
- Petersson, F., Nilsson, A., Holm, C., Jonsson, H. & Laurell, T. (2005) Continuous separation of lipid particles from erythrocytes by means of laminar flow acoustic standing wave forces. *Lab on a Chip*. **5**, 20-22.
- Pfund, D., Rector, D., Shekarriz, A., Popescu, A. & Welty, J. (2000) Pressure drop measurements in a microchannel. *AIChE Journal*. **46**, 1496-1507.
- Phares, D.J., Smedley, G.T. & Zhou, J. (2005) Laminar flow resistance in short microtubes. *International Journal of Heat and Fluid Flow*. **26**, 506-512.
- Press, W.H., Teukolsky, S.A., Vetterling, W.T., & Flannery, B.P. Numerical Recipes in C: The Art of Scientific Computing, Second Edition . New York: Cambridge University Press, 1992.
- Rawool, A., Sushanta, M. & Kandlikar, S. (2006) Numerical simulation of flow through microchannels with designed roughness. *Microfluid Nanofluid*. **2**, 215-221.
- Ren, J., Ganapathysubramanian, B. & Sundararajan, S. (2011) Experimental analysis of the surface roughness evolution of etched glass for micro/nanofluidic devices . *J. Micromech. Microeng.* **21**, 025012.
- Rodriguez, I., Cpicar-Mihalic, P., Kuyper, C., Fiorini, G. & Chiu, D. (2003) Rapid prototyping of glass microchannels. *Analytica Chimica Acta*. **496**, 205--215.
- RoyChaudhuri, C., Dev Das, R., Dey, S. & Das, S. (2011) Functionalized silicon microchannel immunosensor with portable electronic readout for bacteria detection in blood. *Sensors, 2011 IEEE*. 323-326.
- Sasaki, T., Watanabe, M., Hashizume, H., Yamada, H. & Nakazawa, H. (1996) Macromolecule-like aspects for a colloidal suspension of an exfoliated titanate. Pairwise association of nanosheets and dynamic reassembling process initiated from it. *J. Am. Chem. Soc.* **118**, 8329-8335.
- Sikalo, S., Marengo, M., Tropea, C. & Ganic, E.N. (2002) Analysis of impact of droplets on horizontal surfaces. *Experimental Thermal and Fluid Science*. **25**, 503-510.
- Silva, G., Leal, N. & Semiao, V. (2008) Micro-PIV and CFD characterization of flow in a microchannel: velocity profiles, surface roughness and poiseuille numbers. *International J. of Heat and Fluid Flow*. **29**, 1211-1220.

- Singh, S.P. & Mittal, S. (2004) Energy spectra of flow past a circular cylinder. *International Journal of Computational Fluid Dynamics*. **18**, 671-679.
- Sollier, E., Rostaing, H., Pouteau, P., Fouillet, Y. & Achard, J. (1996) Passive microfluidic devices for plasma extraction from whole human blood. *Sensors and Actuators B*. **141**, 617-624.
- Tesduyar, T.E., Mittal, S., Ray, S.E. & Shih, R. (1991) Incompressible flow computations with stabilized bilinear and linear equal-order-interpolation velocity-pressure elements. *Computer Methods in Applied Mechanics and Engineering*. **95**, 221-242.
- Valdes, J., Miana, M., Pelegay, J.L., Nunez, J.L. & Putz, T. (2007) Numerical investigation of the influence of roughness on the laminar incompressible fluid flow through annular microchannels. *International Journal of Heat and Mass Transfer*. **50**, 1865-1878.
- Valdes, J., Miana, M., Martinez, M., Gracia, L. & Putz, T. (2008) Introduction of a length correlation factor for the calculation of laminar flow through microchannels with high surface roughness. *International Journal of Heat and Mass Transfer*. **51**, 4573-4582.
- VanDellnder, V. & Groisman, A. (2006) Separation of plasma from whole human blood in a continuous cross-flow in a molded microfluidic device. *Anal. Chem*. **78**, 3765-3771.
- Xiong, R. (2010) Fluid Flow in Trapezoidal Silicon Microchannels With 3D Random Rough Bottoms. *Journal of Fluids Engineering*. **133**, 031102-1--031102-7.
- Xiong, R. & Chung, J.N. (2010) A new model for three-dimensional random roughness effect on friction factor and heat transfer in microtubes. *International Journal of Heat and Mass Transfer*. **53**, 3284-3291.
- Yager, P., Edwards, T., Fu, E., Helton, K., Nelson, K., Tam, M. & Weigl, B. (2006) Microfluidic diagnostic technologies for global public health. *Nature*. **442**, 412-418.
- Zhang & Sundararajan (2005) The effect of autocorrelation length on the real area of contact and friction behavior of rough surfaces. *Journal of Applied Physics*. **97**, 103526-1--103526-7.
- Zhu, L., Tretheway, D., Petzold, L. & Meinhart, C. (2005) Simulation of fluid slip at 3D hydrophobic microchannel walls by the lattice Boltzmann method. *Journal of Computational Physics*. **202**, 181-195.

CHAPTER 4. GENERAL CONCLUSIONS

General Discussion

The study in Chapter 2 has shown that the effect of stochastic nano-scale surface roughness on microfluidic flow can be studied using computational fluid dynamic DNS simulations. Additionally, we have shown that validation between micro-PIV experiments and a large DNS simulation is possible using autocorrelation length and energy spectra. CFD analysis lends to a deeper understanding of the characterization of the fluid flow within the microchannel, and the highly resolved DNS simulations reveal the flow to be characterizable. We show that for a range of flow rates that are diffusion dominated, the energy transfer is consistently characterizable. Autocorrelation and velocity contour analyses showed that the nano-scale surface roughness produced small structures that combine and persist well above the rough surface. In addition, the energy spectra analyses show the small eddies produced by the etched surface give rise to higher energy eddies that decay more slowly than eddies produced by the un-etched surface.

Chapter 3 was very similar in style and analysis to Chapter 2 with the exception of the larger experimental surface used for the etched and un-etched microchannels. The analyses were performed the same way for both Chapter 2 and 3, but the autocorrelation length and energy spectra results were slightly different. The conclusions drawn from both sets of results, however, were the same. The size of the microchannel surface has some effect on the fluid flow characterization results. More investigation in the future with difference surface sizes might reveal the effect from this change.

The chemical etching surface treatment and other stochastic rough surfaces, even at the nano-scale, can be characterized and potentially be harnessed across a range of fluid flow rates. Devices that use microchannels such as lab-on-a-chip medical devices can therefore be tuned and optimized for their respective applications such as reagent mixing, bubble creation and transport, fluid transport, cell manipulation using stochastic surface roughness.

Recommendations for Future Research

General Recommendations

The depth of correlation associated with the micro-PIV experiments in Chapter 2 limited the flow visualization near the rough surface. Smaller seeding particles may be needed, or equipment to reduce the depth of correlation may be necessary. Other techniques such as molecular tagging velocimetry (MTV) (Gendrich et al. (1997)) might be more suitable for investigation of flow effects near the rough surface (less than $5\mu\text{m}$ above the rough surface).

Eddies created by the surface roughness were seen to induce a certain amount of mixing. Other than the energy cascade seen from the energy spectra analyses, a tangible mixing metric was not investigated in this thesis. The mixing effect produced by the roughness is worth quantitatively investigating for use in biomedical lab-on-a-chip devices. The surface roughness height may need to be increased to realistically mix difference species for certain microchannel lengths. This could easily be achieved by increasing the HF-acid etching time to more than 30 minutes.

Non-Newtonian Fluid Recommendation

A very limited amount of work has been done focusing on the effect of roughness on microchannel pressure-driven flow of non-Newtonian fluids specifically, which describes many biofluids important to microfluidic medical devices such as blood, synovial fluid, and others. Some studies have suggested that surface roughness plays a considerable role in the flow structure more dramatically compared to Newtonian fluids, but very few have extracted quantitative effects from surface roughness on non-Newtonian fluid flows. Martanto et al. (2005) looked at the flow of water and blood in microneedles and found an 11% mean absolute percent error between experiments and simulations where the surface roughness was neglected (considered ideally smooth). Martanto et al. (2005) concluded that the 100nm surface roughness height could contribute to the difference between simulations and

experiments. Bulk flow measurements were performed on a microchannel where whole horse blood flowed through a microchannel with measured surface roughness by Prentner et al. (2010). It was found that the apparent viscosity decreased from 10.7 mPa.s to 6.5 mPa.s when the surface roughness increased from 60nm to 1.8µm for the same pressure driven flow. The shear thinning nature of blood seemed to be enhanced by the increase in surface roughness.

For a non-Newtonian-fluid analyses assuming constant temperature, incompressible, steady state, laminar flow, conservation of mass and momentum are represented by the generalized Newtonian equations (17) and (18), respectively.

$$\nabla \cdot \mathbf{u} = 0 \quad (17)$$

$$\rho \left(\frac{\partial \mathbf{u}}{\partial t} + \mathbf{u} \cdot \nabla \mathbf{u} \right) = -\nabla p + \nabla \cdot \boldsymbol{\tau} + \eta \nabla^2 \mathbf{u} \quad (18)$$

Where \mathbf{u} is the velocity, p is the pressure, ρ is the fluid density, $\boldsymbol{\tau}$ is the stress tensor, and η is the apparent viscosity. For a non-Newtonian, the last three terms are replaced by $\nabla \cdot [\eta(\nabla \mathbf{u} + \nabla \mathbf{u}^T)]$ where the apparent viscosity is a function of shear rate, $\dot{\gamma}$, represented by the Carreau-Yasuda model from Bird et al.(1987) in equation (19). The Carreau-Yasuda model has been shown as a good estimation for blood viscosity (Gijssen et al. (1999)) and other shear-thinning fluids (Bird et al. (1987)).

$$\frac{\eta - \eta_{\infty}}{\eta_0 - \eta_{\infty}} = [1 + (\lambda \dot{\gamma})^a]^{(n-1)/a} \quad (19)$$

Where η_0 is the zero-shear-rate viscosity, η_{∞} is the infinite-shear-rate viscosity, λ is the time constant, and n is the power-law exponent.

The velocity field of blood, a shear-thinning biofluid, is difficult to measure with micro-PIV experiments due refractive-index matching, clotting, and its translucency (Gijssen et al. (1999)). As a result, “blood analog” fluids are used to simulate the rheological properties of blood in experiments where flow visualization is paramount. Solutions of

xanthan gum, potassium thiocyanate, and polyacrylamide (PAA) dissolved in water have been used as blood analog fluids in studies by Gijzen et al. (1999), Sousa et al. (2011), and Bandulasena et al. (2011). The values used for the Carreau-Yasuda model by Gijzen et al. (1999) are given in table Table 3. The values are derived from a blood analog made by dissolving a combination of potassium thiocyanate and xanthan gum in water (named KSCN-X), which Gijzen et al. (1999) showed to follow the shear-thinning properties of blood well under normal flow conditions experienced in vascular systems.

Table 3. Fluid properties of non-Newtonian blood analog fluid KSCN-X solution by Gijzen et al. (1999)

Zero-shear-rate viscosity, η_0 [Pa s]	0.022
Infinite-shear-rate viscosity, η_∞ [Pa s]	0.0022
Time constant, λ [s]	0.110
Transition parameter, a	0.644
Power-law index, n	0.392
Density, ρ [kg/m ³]	1410

References

- Bandulasena, H.C.H., Zimmerman, W.B., & Rees, J.M. (2011) An inverse method for rheometry of power-law fluids. *Measurement Science and Technology*. **22**, 125402.
- Bird, R.B., Armstrong, R.C., & Hassager, O. (1987) Dynamics of Polymeric Liquids. **vol. 1**. 2nd ed. Wiley, New York.
- Gendrich, C.P., Koochesfahani, M.M., Nocera, D.G. (1997) Molecular tagging velocimetry and other novel applications of a new phosphorescent supramolecule. *Experiments in Fluids*. **23**, 361-372.

- Gijsen, F.J.H., van de Vosse, F.N., & Janssen, J.D. (1999) The influence of the non-Newtonian properties of blood on the flow in large arteries: steady flow in a carotid bifurcation model. *J. of Biomechanics*. **32**; 6, 601-608.
- Martanto, W., Baisch, S.M., Costner, E.A. & Prausnitz, M.R. (2005) Fluid dynamics in conically tapered microneedles. *AIChE Journal*. **51** No. 6, 1599-1607.
- Prentner, S., Allen, D.M., Larcombe, L., Marson, S., Jenkins, K., & Saumer, M. (2010) Effects of channel surface finish on blood flow in microfluidic devices. *Microsyst Technol*. **16**, 1091-1096.
- Sousa, P.C., Pinho, F.T., Oliveira, M.S.N., & Alves, M.A. (2011) Extensional flow of blood analog solutions in microfluidic devices. *Biomicrofluidics*. **5**, 014108.

APPENDIX A. MICROCHANNEL AND SURFACE CREATION

The microchannel construction is based on a lithography process with SU-8 photoresist and poly(dimethylsiloxane) (PDMS). Figure 17 depicts a cross-sectional view of a simplified step-by-step process of the microchannel fabrication with an etched bottom surface. To create the microchannel, SU-8 is applied to a silica substrate (b). Then, UV light is shown onto the photoresist through a mask which depicts the microchannel network (c). Next, the non-UV-exposed photoresist is removed, and the mold for the microchannel is complete (d). Liquid PDMS is then cast around the mold, set to cure, and finally removed from the mold to reveal the actual microchannel (f). Steps (a) through (f) result in a three-sided, non-enclosed microchannel.

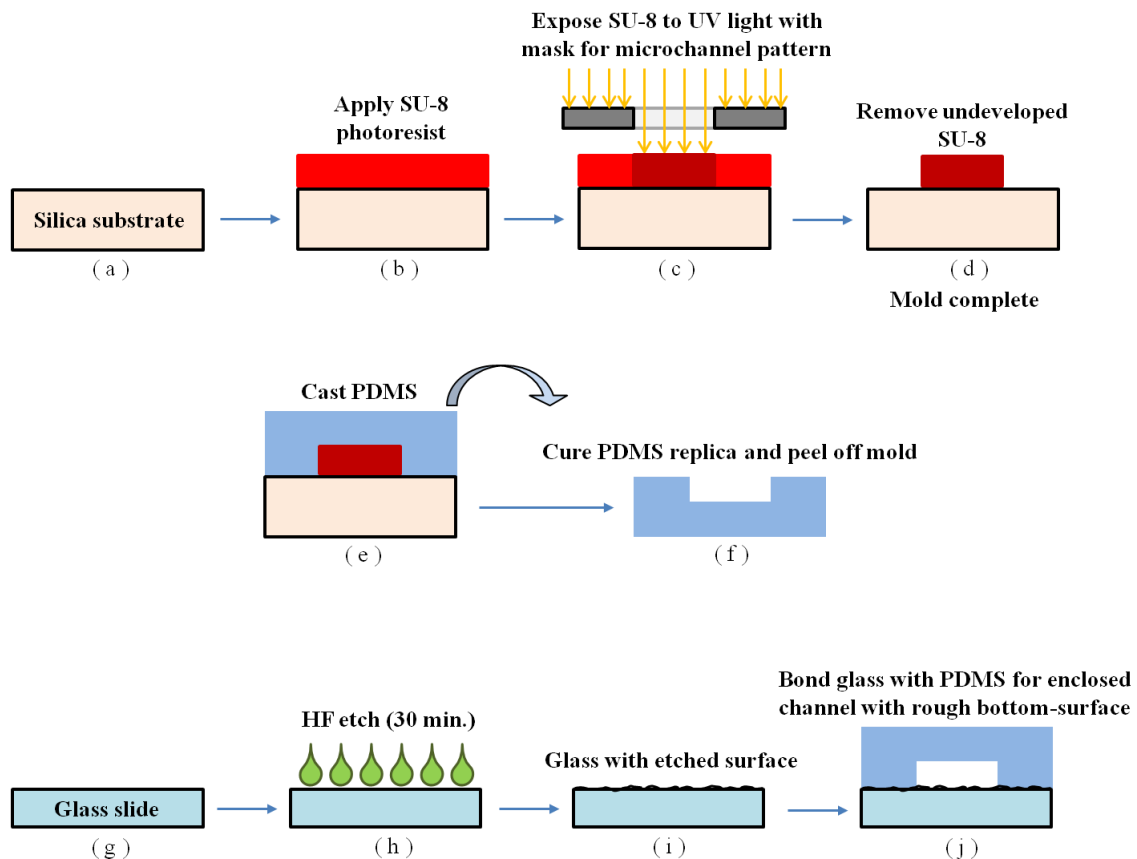


Figure 17. Sequential process to manufacture the experimental microchannel with etched glass as the bottom surface

The novel aspect of this research revolves around the use of genuine surface topography in the computational domain. Previous studies have all looked at periodic, ordered surfaces, or they have used surfaces that are random, but they do not represent a real surface (as mentioned in the Introduction of Chapter 3). The fabricated rough surface of the microchannel is constructed beginning with a glass slide. Then, one of the sides of the glass slide is etched using hydrofluoric acid for 30 minutes (h). Any etching time longer than 30 minutes reduces the transparency of the glass needed for micro-PIV experiments (longer etching times resulting in higher surface roughness are possible, but they are not investigated in this thesis). After etching is complete, the glass slide is rinsed with deionized water, dried, and plasma bonded to the PDMS to form the fourth, enclosed surface of the microchannel (j). Figure 18 shows single optical profilometer scans of both etched and un-etched glass used in both studies.

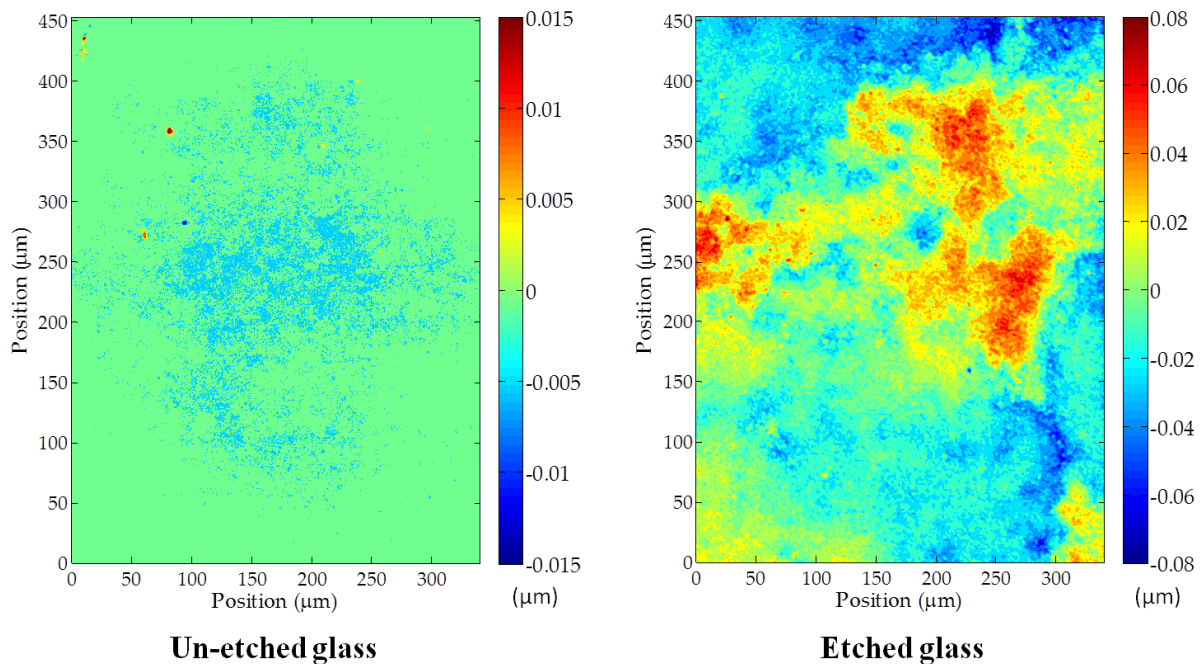


Figure 18. Sample optical profilometer surface scans of un-etched glass (left) and etched glass (right)

The second study in Chapter 3 uses a longer, non-repetitive rough surface in the computational microchannel domain. The scan area of the optical profilometer was limited to $460\mu\text{m} \times 350\mu\text{m}$. Therefore, side-by-side images needed to be stitched together to form one continuous surface. Figure 20 shows two optical profilometer scans that were taken consecutively with a small overlapping region (about 25% of the length of the scan) highlighted in grey. The overlapping region in Figure 20 is the true overlap position needed for a continuous surface, but the exact size of the region was not needed *a priori* in order to stitch the images together.

A brute force cross-correlation method was used to find the correct overlap between consecutive images. The norm used for finding the exact overlap between consecutive images of $N \times M$ (row x column) dimension is outlined below and depicted in Figure 19 for an $I \times J$ test region (the norm was calculated using Matlab®):

$$\text{Overlap Test Region} = \frac{1}{I * J} \sum_i^I \sum_j^J |\text{Scan 1 Test Region}_{ij} - \text{Scan 2 Test Region}_{ij}|$$

The overlap test region is shifted for each scan overlap possibility (the red highlighted region in Figure 19 depicts one test instance). The minimum valued test region defines the region of best fit and gives a position (or translation length) for which the consecutive scans can be overlaid.

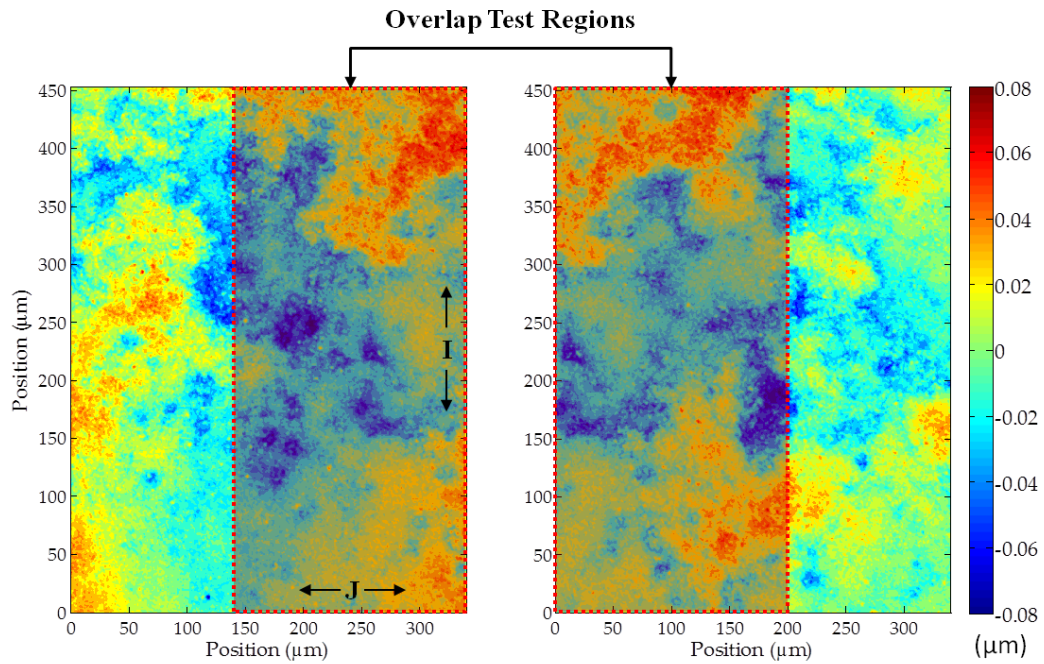


Figure 19. Consecutive surface scans with a sample test region (shaded in red)

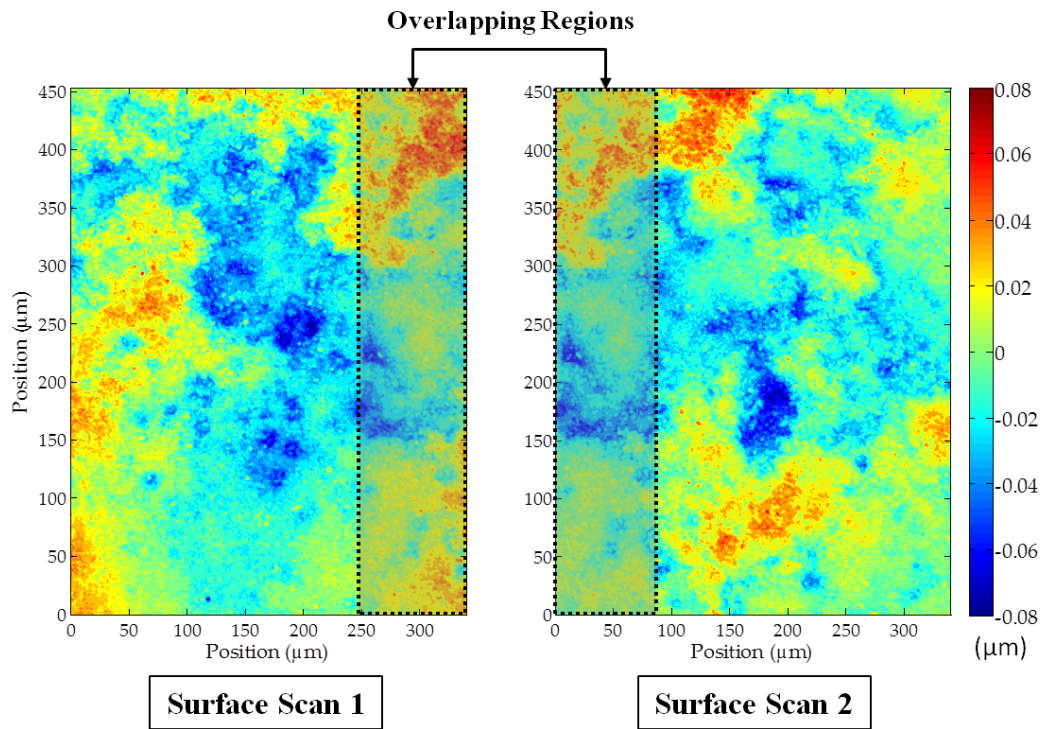


Figure 20. Consecutive surface scans showing the true overlapping regions (shaded)

Once the true overlapping region is known, the two consecutive images are tested for a planar fit. Each image is tilted through a small range to find the optimal tilt match. Once the tilted images are matched optimally, the image scans are stitched together to form a continuous surface. The etched and un-etched glass surfaces used in Chapter 3's study consist of three images stitched together. The etched surface used in the second study is shown in Figure 21, which also shows the individual images stitched together to make the continuous surface. Figure 22 shows the whole surface used in Chapter 3 for the bottom, rough etched surface. The un-etched surface underwent the same stitching procedure, but it is not shown here explicitly.

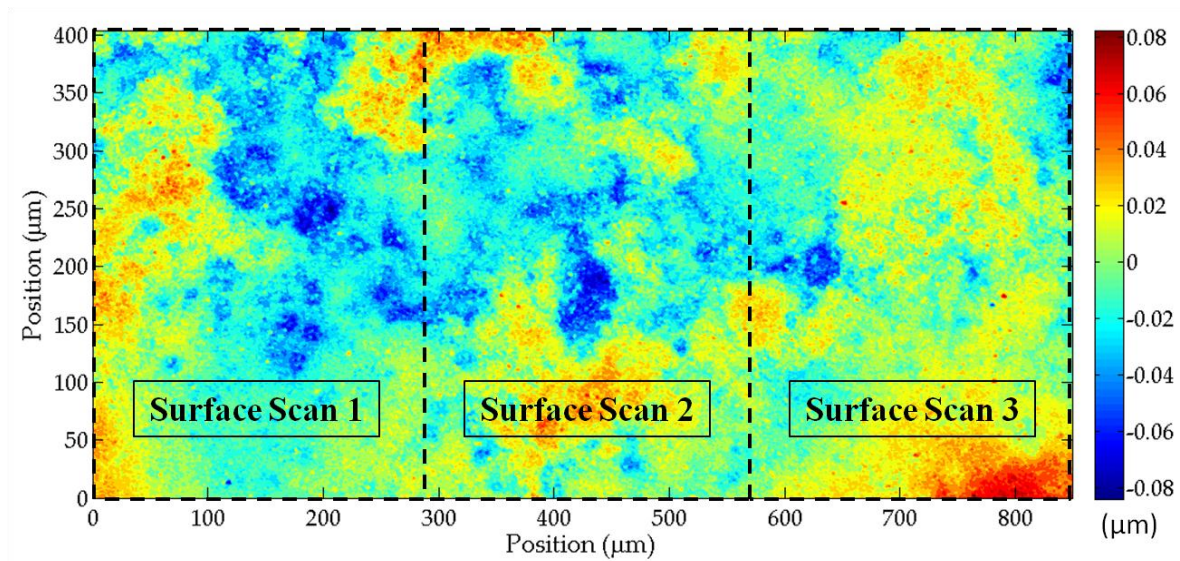


Figure 21. Three consecutive surface scans seen stitched together with dotted lines showing the original scans

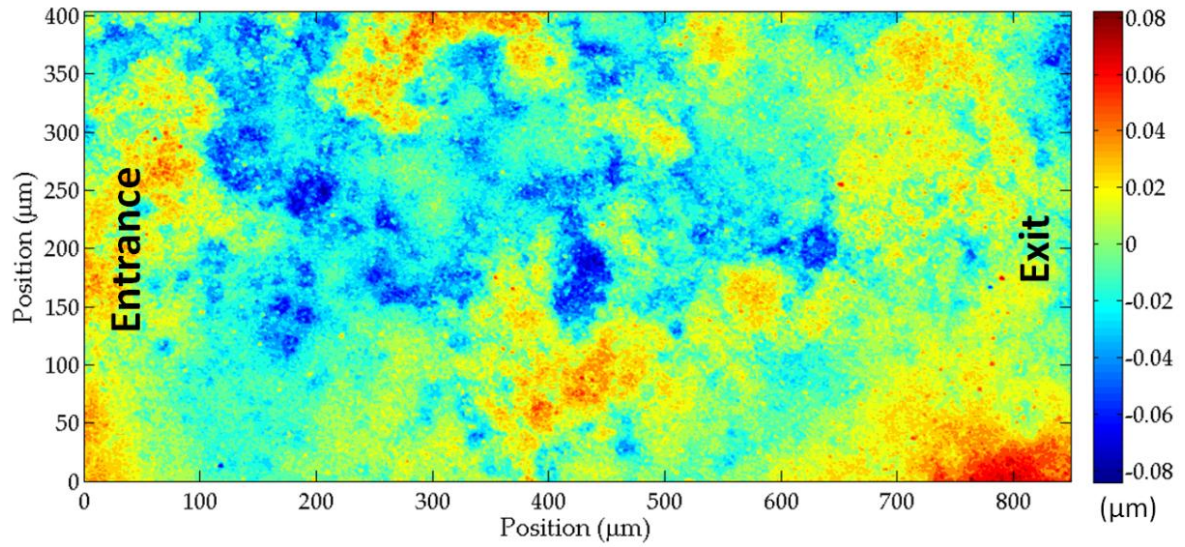
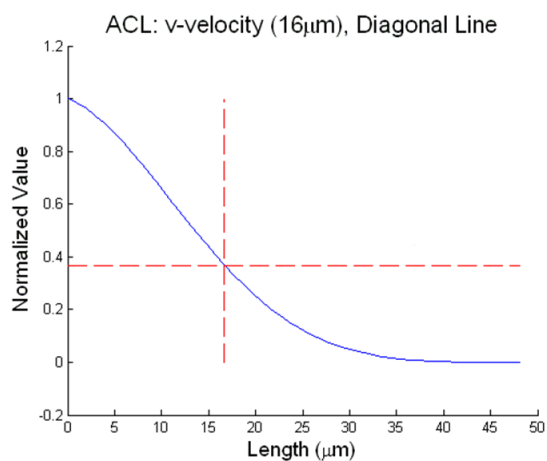
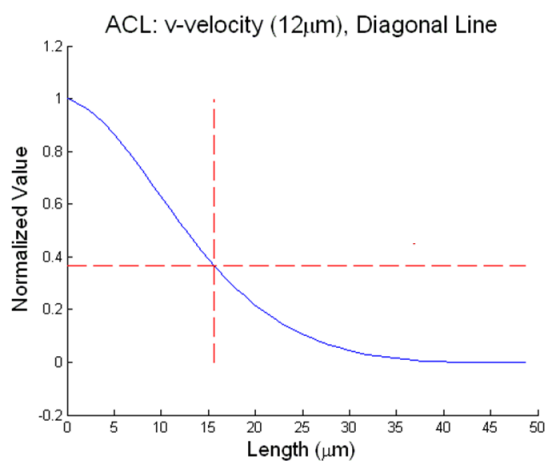
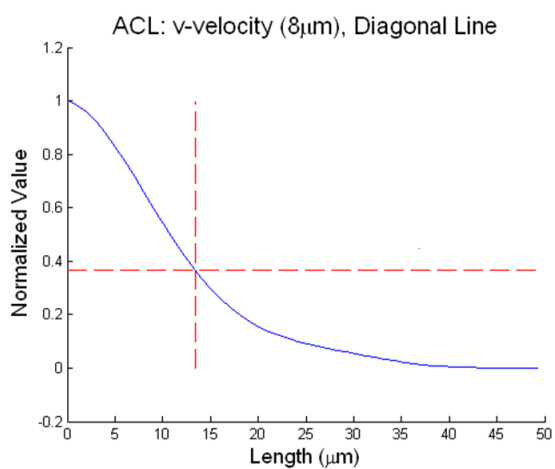
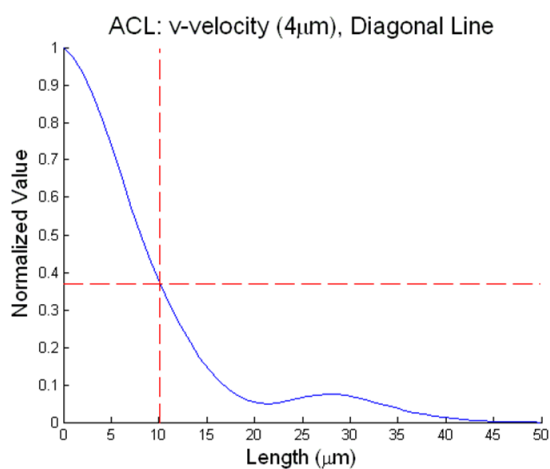
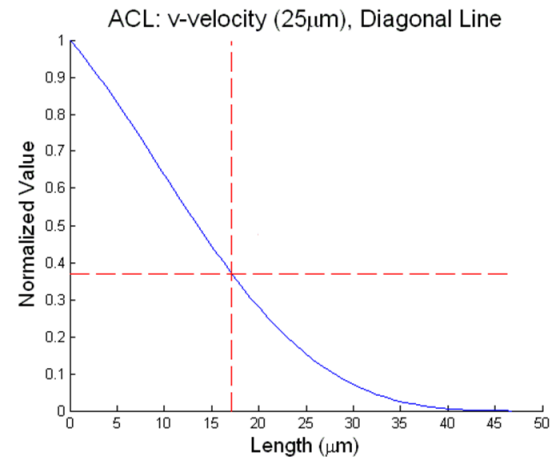
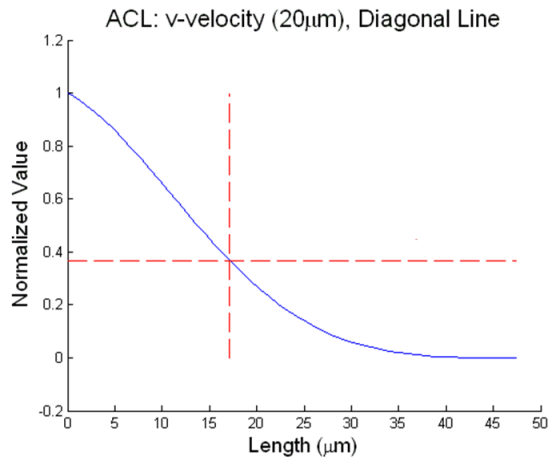


Figure 22. Final etched microchannel surface with three consecutive images.

APPENDIX B. AUTOCORRELATION FUNCTIONS

The figures below are the autocorrelation functions from which the autocorrelation length was derived for the v-velocity perturbation component at multiple heights above the rough surface.





ACKNOWLEDGEMENTS

I would first like to acknowledge the guidance of my major professor, Dr. Baskar Ganapathysubramanian. He has been instrumental in motivating me in order to grow and succeed during my graduate school career.

Secondly, I need to thank my research group for their support and critiques, and to especially thank my colleague Yu Xie for his help with the CFD simulations on CyStorm. I would also like to thank Jing Ren for her experimental micro-PIV collaboration as well as my program of study committee, Dr. Michael G. Olsen and Dr. Sriram Sundararajan, for their critique, direction, and suggestions.

Lastly, I would be remiss if I did not acknowledge all the love and encouragement from my family and friends over the past two years. Without the support of all those mentioned above, none of this would have been possible.